

Key Material Properties for Thermo-Structural Analysis of Transformational Challenge Reactor Core Components



D. Schappel
K. A. Terrani

August 2019

M3CT-19OR06090119

DOCUMENT AVAILABILITY

Reports produced after January 1, 1996, are generally available free via US Department of Energy (DOE) SciTech Connect.

Website www.osti.gov

Reports produced before January 1, 1996, may be purchased by members of the public from the following source:

National Technical Information Service
5285 Port Royal Road
Springfield, VA 22161
Telephone 703-605-6000 (1-800-553-6847)
TDD 703-487-4639
Fax 703-605-6900
E-mail info@ntis.gov
Website <http://classic.ntis.gov/>

Reports are available to DOE employees, DOE contractors, Energy Technology Data Exchange representatives, and International Nuclear Information System representatives from the following source:

Office of Scientific and Technical Information
PO Box 62
Oak Ridge, TN 37831
Telephone 865-576-8401
Fax 865-576-5728
E-mail reports@osti.gov
Website <http://www.osti.gov/contact.html>

This report was prepared as an account of work sponsored by an agency of the United States Government. Neither the United States Government nor any agency thereof, nor any of their employees, makes any warranty, express or implied, or assumes any legal liability or responsibility for the accuracy, completeness, or usefulness of any information, apparatus, product, or process disclosed, or represents that its use would not infringe privately owned rights. Reference herein to any specific commercial product, process, or service by trade name, trademark, manufacturer, or otherwise, does not necessarily constitute or imply its endorsement, recommendation, or favoring by the United States Government or any agency thereof. The views and opinions of authors expressed herein do not necessarily state or reflect those of the United States Government or any agency thereof.

Transformational Challenge Reactor Program

**KEY MATERIAL PROPERTIES FOR THERMO-STRUCTURAL ANALYSIS OF
TRANSFORMATIONAL CHALLENGE REACTOR COMPONENTS**

D. Schappel
K. A. Terrani

Date Published: August 2019

Milestone M3CT-19OR06090119

Prepared by
OAK RIDGE NATIONAL LABORATORY
Oak Ridge, Tennessee 37831-6283
managed by
UT-BATTELLE, LLC
for the
US DEPARTMENT OF ENERGY
under contract DE-AC05-00OR22725

CONTENTS

List of Figures	v
Abstract	vii
1. Introduction	1
2. Material Correlations	2
2.1 Uranium dioxide	2
2.1.1 Thermal Conductivity	2
2.1.2 Specific Heat	3
2.1.3 Creep	4
2.1.4 Swelling	5
2.1.5 Coefficient of Thermal Expansion	5
2.1.6 Initial Density	6
2.1.7 Elastic Properties	6
2.2 Stainless Steel 316	6
2.2.1 Thermal Conductivity	6
2.2.2 Specific Heat	6
2.2.3 Coefficient of Thermal Expansion	7
2.2.4 Initial Density	7
2.2.5 Plasticity	7
2.2.6 Elastic Properties	8
2.3 SiC and SiC with Embedded TRISO	8
2.3.1 Thermal Conductivity	8
2.3.2 Specific Heat	9
2.3.3 Swelling	10
2.3.4 Coefficient of Thermal Expansion	11
2.3.5 Creep	12
2.3.6 Initial Density	12
2.3.7 Elastic Properties	12
3. Methods	13
4. Results	15
4.1 SiC Can Variations	15
4.1.1 Thermal Conductivity	16
4.1.2 Coefficient of Thermal Expansion	17
4.1.3 Elastic Modulus	17
4.1.4 Poisson's Ratio	19
4.1.5 Swelling	20
4.2 SiC-Fueled Material Variations	21
4.2.1 Thermal Conductivity	21
4.2.2 Coefficient of Thermal Expansion	22
4.2.3 Elastic Modulus	23
4.2.4 Poisson's Ratio	24
4.2.5 Swelling	25
4.3 Stainless Steel 316L	26
4.3.1 Interface Heat Transfer Coefficient	27
4.3.2 Thermal Conductivity	28
4.3.3 Coefficient of Thermal Expansion	29
4.3.4 Elastic Modulus	29
4.3.5 Poisson's Ratio	30
4.4 Uranium dioxide	31

4.4.1	Thermal Conductivity.....	31
4.5	Geometry and Modeling Methods.....	31
4.5.1	Silicon Carbide Can.....	31
4.5.2	One-Dimensional Analysis.....	35
4.5.3	TRISO Cavities.....	36
5.	Conclusion.....	39
6.	References.....	40

LIST OF FIGURES

Figure 1. General description of the bristle wall concept that constitutes the interface layer between the UO_2 fuel and the SS316L can.	1
Figure 2. UO_2 thermal conductivity at a porosity of 5%.	3
Figure 3. UO_2 specific heat versus temperature.	4
Figure 4. UO_2 swelling versus burnup and temperature.	5
Figure 5. Plot of the SS316L thermal conductivity versus temperature.	6
Figure 6. Plot of the SS316L specific heat versus temperature.	7
Figure 7. Plot of the SS316L yield stress versus plastic strain.	8
Figure 8. Plots of the thermal conductivities for SiC versus temperature and fluence.	9
Figure 9. Plot of the SiC-specific heat versus temperature.	10
Figure 10. Plots of the SiC swelling versus fluence and temperature. (a) Linear/log scale. (b) Linear/linear scale and the addition of the 1250 °C trend.	11
Figure 11. Plot of the SiC CTE.	12
Figure 12. Representations of the meshes used for the sensitivity studies. Blue is the can, red is the interface layer, and green is the fuel. (a) UO_2 exterior view. (b) UO_2 cross section. (c) SiC exterior view. (d) SiC cross-section view.	14
Figure 13. Maximum principal stress profiles in the SiC sensitivity study geometry using nominal values. (a) Thermal stresses after the power ramp. (b) Mostly swelling stresses at the saturation of the swelling.	15
Figure 14. Largest maximum principal stress as a result of varying the thermal conductivity in the can. (a) Maximum principal stress in the can. (b) Maximum principal stress in the fueled region.	16
Figure 15. Largest maximum principal stress as a result of varying the CTE in the can. (a) Maximum principal stress in the can. (b) Maximum principal stress in the fueled region.	18
Figure 16. Largest maximum principal stress as a result of varying the elastic modulus in the can. (a) Maximum principal stress in the can. (b) Maximum principal stress in the fueled region.	19
Figure 17. Largest maximum principal stress as a result of varying the Poisson's ratio in the can. (a) Maximum principal stress in the can. (b) Maximum principal stress in the fueled region.	20
Figure 18. Largest maximum principal stress as a result of varying the irradiation swelling in the can. (a) Maximum principal stress in the can. (b) Maximum principal stress in the fueled region.	21
Figure 19. Largest maximum principal stress as a result of varying the thermal conductivity in the fueled region. (a) Maximum principal stress in the can. (b) Maximum principal stress in the fueled region.	22
Figure 20. Largest maximum principal stress as a result of varying the CTE in the fueled region. (a) Maximum principal stress in the can. (b) Maximum principal stress in the fueled region.	23
Figure 21. Largest maximum principal stress as a result of varying the elastic modulus in the fueled region. (a) Maximum principal stress in the can. (b) Maximum principal stress in the fueled region.	24
Figure 22. Largest maximum principal stress as a result of varying Poisson's ratio in the fueled region. (a) Maximum principal stress in the can. (b) Maximum principal stress in the fueled region.	25
Figure 23. Largest maximum principal stress as a result of varying Poisson's ratio in the fueled region. (a) Maximum principal stress in the can. (b) Maximum principal stress in the fueled region.	26

Figure 24. Temperature and stress profile in the SS316L can as a result of thermal expansion at 100 W/cm ³ . (a) Temperature profile. (b) Von Mises stress profile. (c) Hoop stress cross section. (d) Von Mises stress cross section.	27
Figure 25. (a) Maximum Von Mises stress in the SS316L can as a result of varying the interface HTC. (b) Maximum Von Mises stress in the SS316L can as a result of varying the side interface HTC while the bottom surface was held at 200W/m ² -K.	28
Figure 26. Plot of the maximum Von Mises stress in the SS316L can as a result of varying the SS316L thermal conductivity.	29
Figure 27. Plot of the maximum Von Mises stress in the SS316L can as a result of varying the SS316L CTE.	29
Figure 28. Plot of the maximum Von Mises stress in the SS316L can due to varying the elastic modulus.	30
Figure 29. Plot of the maximum Von Mises stress in the SS316L can due to varying Poisson's ratio.	30
Figure 30. Plot of the maximum Von Mises stress in the SS316L can due to varying the UO ₂ thermal conductivity.	31
Figure 31. Y mesh geometries used for estimating the effect of completely homogenizing the SiC geometries. (a) Outer view. (b) Cross section view.	32
Figure 32. Temperature cross-section profiles of the Y mesh simulations at swelling saturation. (a) Temperature profile for the first simulation with nominal material values in the can and fueled regions. (b) Temperature profile for the second simulation with the same properties in both regions. (c) Temperature profile for heat generation in all regions at 50W/cm ³ . (d) Temperature profile for heat generation in all regions at 27.27W/cm ³	33
Figure 33. Maximum principal stress profiles at the end of the power ramp. (a) Stress profile for the first simulation with nominal material values in both regions. (b) Stress profile for the second simulation with the same material properties in both regions. (c) Stress profile for heat generation in all regions at 50W/cm ³ . (d) Stress profile for heat generation in all regions at 27.27W/cm ³	34
Figure 34. Maximum principal stress profiles at a fluence of 1 × 10 ²⁵ n/m ² . (a) Stress profile for the first simulation with nominal material properties. (b) Stress profile for the second simulation with the same material properties on both regions. (c) Stress profile for heat generation in all regions at 50W/cm ³ . (d) Stress profile for heat generation in all regions at 27.27W/cm ³	35
Figure 35. Geometry of the pellet with TRISO cavities.	37
Figure 36. Plots of the temperature and maximum principal stress. Left is the solid cylinder results. Right are the results for the pellet with TRISO cavities. (a) and (b) Temperature profiles. (b) and (c) Stress profiles after the power ramp. (e) and (f) Stress profiles at swelling saturation.	38

ABSTRACT

This report presents thermo-structural (Williamson 2012) constitutive relationships and models pertaining to Transformational Challenge Reactor (TCR) core components using BISON. The material correlations for TCR core candidate materials include 316L stainless steel, uranium dioxide, and Chemical Vapor Infiltrated (CVI) silicon carbide were compiled. Preliminary, sensitivity analyses were performed on a simple cylindrical geometry by parametrically varying material properties. The sensitivity analyses elucidate the impact of material properties on the induced stresses in the TCR core structures. The results of the sensitivity studies for the SiC concept showed that the swelling is expected to be the largest source of uncertainty, followed by the elastic modulus. In the SS316L and UO₂ concept, the thermal conductivity of the can was the dominate effect, and a temperature dependent correlation or tabulated data would be advisable. The geometry and modeling method simulations showed that the inclusion of the heat generation in the SiC can does alter the stress and temperature magnitudes. However, the stress concentrations and profiles remain consistent.

Additional simulations were performed to investigate the effects of modeling simplifications such as heat generation in the SiC can and neglecting the TRI-structural ISotropic particle cavities within the SiC fueled region. It was found that although the magnitudes of the temperatures and stresses did change noticeably, the general trends regarding the temperature and stress profiles, and locations of the maximum stresses did not change significantly. These are highly relevant results for the more complicated geometries that are targeted by TCR.

1. INTRODUCTION

BISON, developed by the US Department of Energy–Nuclear Energy (DOE-NE) Nuclear Energy Advanced Modeling and Simulation (NEAMS) (Williamson 2012) and maintained by Idaho National Laboratory, is a finite-element fuel performance code that is capable of predicting a significant range of physical effects. For the Transformational Challenge Reactor (TCR) project, BISON is being used to predict the temperatures and stresses in various fuel candidates to be advanced manufactured into complex geometries. BISON has also been used to investigate the sensitivity of the fuel’s performance to its material properties. A significant section of this report focuses on the effects on the stress by varying one material property while maintaining all other properties at their nominal conditions. In this way, it is possible to determine which material properties should be measured more accurately and which properties are largely unimportant or already satisfactorily known for the expected operating conditions.

Two different fuel concepts were considered in these simulations. The first being tristructural isotropic (TRISO) particles dispersed inside a monolithic silicon carbide (SiC) matrix surrounded and integrated with a fuel-free SiC shell or can on all sides. Details of the SiC-based fuel manufacturing process are described in another TCR milestone report (Trammell 2016). The second fuel concept is uranium dioxide (UO₂) fuel with a 316L stainless steel (SS316L) can and SS316L bristles or springs between the UO₂ and SS316L can (Figure 1). In the simulations, the bristles are modeled as a 1 mm thick interface layer, which is given approximate material property values.

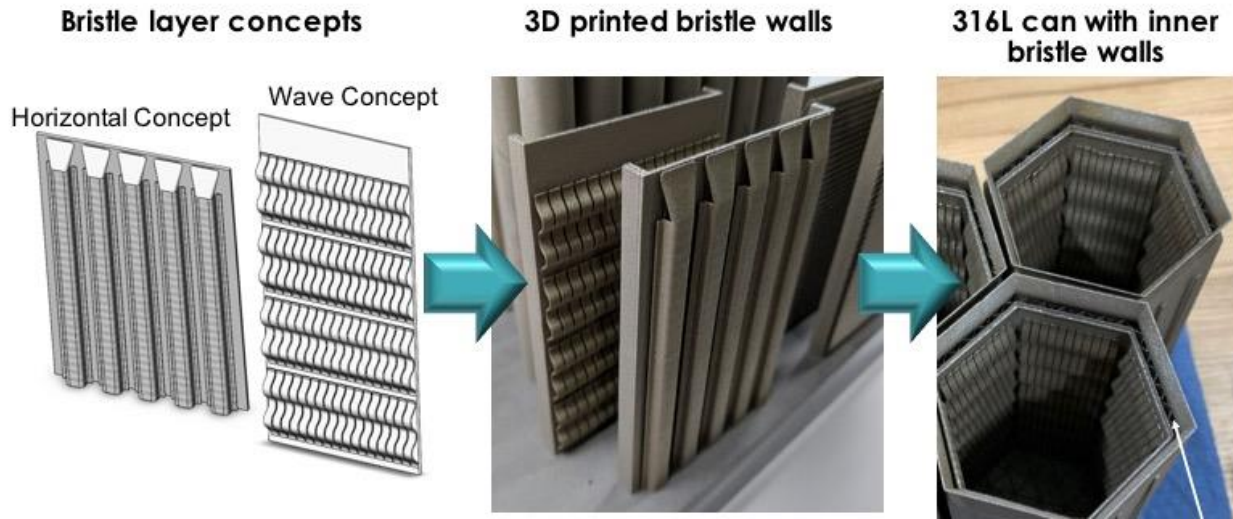


Figure 1. General description of the bristle wall concept that constitutes the interface layer between the UO₂ fuel and the SS316L can.

Most of the correlations in the materials sections are pulled from the correlations already present in BISON materials files. However, several material properties were added or edited for the SiC and SS316L. The most notable of these is the SS316L plasticity model. This model is used to estimate the amount of plastic strain and the potential for failure of the stainless steel can. It uses an explicit formulation and a Von Mises yielding criterion. However, plasticity is not included in the SS316L sensitivity studies. With plasticity enabled, the can will generally yield because of thermal expansion and then deform until the thermal expansion has been accommodated. As a result, these plasticity simulations were not very helpful in determining the stress’s sensitivity to material properties. However, the ability to include plasticity in the model, is useful in determining the deformation and estimated failure of the

SS316L can. Thus, the plasticity is included in the list of materials, but a sensitivity study was not performed for this property.

Additional simulations were performed to investigate the effects of certain modeling simplifications. These simplifications have the potential to significantly reduce the computational requirements and increase the range of geometries that can be meshed for use in BISON. These simplifications are the presence of TRISO cavities in the fueled SiC region and neglecting the discrete modeling of the SiC can and fueled region, respectively.

This report is divided into four sections. The material correlation section describes the selected nominal correlations. The methods section describes the simulations used for the sensitivity studies. The results section covers these simulations and their findings, and the conclusion section summarizes the results and their implications.

2. MATERIAL CORRELATIONS

2.1 URANIUM DIOXIDE

2.1.1 Thermal Conductivity

The Fink-Lucuta model was used for UO₂ thermal conductivity (Fink 2000, Lucuta 1996). The base equation is shown in Equation 1.

$$k = k_0 * fd * fp * fb * fr , \quad (1)$$

where k is the thermal conductivity (W/m-K), k₀ is the unirradiated thermal conductivity, fd is the dissolved fission product factor (-), fp is the precipitated fission product factor (-), fb is the bubble factor (-), and fr is the radiation damage factor (-).

The unirradiated thermal conductivity is given by Equation 2.

$$k_0 = \left[\frac{100}{7.5408 + 17.692 \frac{T_K}{1000} + 3.6142 \left(\frac{T_K}{1000} \right)^2} + \frac{6400}{\left(\frac{T_K}{1000} \right)^{2.5}} \text{EXP} \left(- \frac{16350}{T_K} \right) \right] \frac{1}{1 - \left(2.6 - 0.5 \frac{T_K}{1000} \right) 0.05} , \quad (2)$$

where k₀ is the unirradiated thermal conductivity (W/m-K) and T_K is the temperature (K). The factors are given by Equations 3 through 6.

$$fd = \left(\frac{1.09}{B^{3.265}} + 0.0643 \sqrt{\frac{T_K}{B}} \right) \text{atan} \left(\frac{1}{\frac{1.09}{B^{3.265}} + 0.0643 \sqrt{\frac{T_K}{B}}} \right) , \quad (3)$$

where fd is the dissolved fission product factor (-), T_K is the temperature (K), and B is the burnup (% fissions per initial metal atom [FIMA]).

$$fp = 1 + \left(\frac{0.019B}{3-0.019B} \right) \left[\frac{1}{1+EXP\left(\frac{-T_K-1200}{100}\right)} \right], \quad (4)$$

where fp is the precipitated fission product factor (-), B is the burnup (%FIMA), and T_K is the temperature (K).

$$fb = \frac{1-P}{1+0.5P}, \quad (5)$$

where fb is the bubble factor (-) and P is the porosity (-).

$$fr = 1 - \frac{0.2}{1+EXP\left(\frac{T_K-900}{80}\right)}, \quad (6)$$

where fr is the radiation damage factor (-), and T_K is the temperature (K). The previous “fr” and “fp” are sigmoid-shaped functions, with a transition between about 800 and 1,000K. When all of the factors are multiplied together, there is a slight increase in thermal conductivity from 800 to 1,000K before it resumes its downward trend. Figure 2 shows the UO₂ thermal conductivity trends.

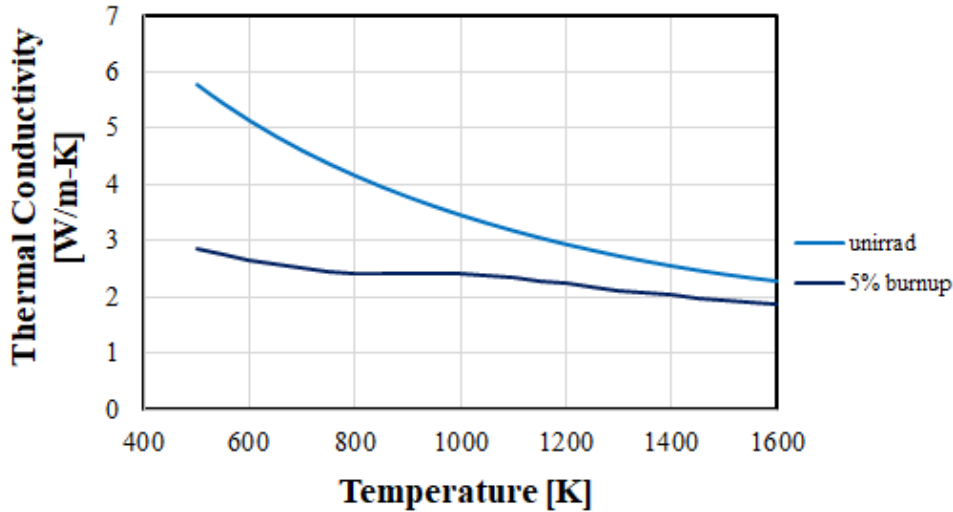


Figure 2. UO₂ thermal conductivity at a porosity of 5%.

2.1.2 Specific Heat

The UO₂ specific heat is given by Equation 7 (Fink 2000).

$$c_p = \frac{1}{0.27} \left(52.1743 + 87.95 \frac{T_K}{1000} - 84.2411 \frac{T_K^2}{1000} + 31.542 \frac{T_K^3}{1000} - 2.6337 \frac{T_K^4}{1000} - \frac{0.71391}{\left(\frac{T_K}{1000}\right)^2} \right), \quad (7)$$

where c_p is the specific heat (J/kg-K) and T_K is the temperature (K). Figure 3 plots the equation; the results are approximately constant with values between 280 and 340J/kg-K.

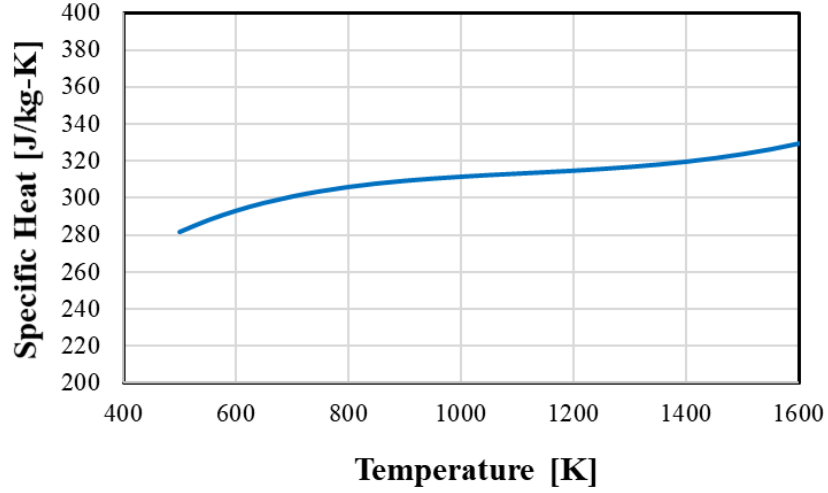


Figure 3. UO₂ specific heat versus temperature.

2.1.3 Creep

The UO₂ creep is given by Equation 8 (Allison 1993).

$$\dot{\epsilon} = \frac{A_1 + A_2 f''' }{(A_3 + D)G^2} \sigma * EXP\left(-\frac{Q_1}{RT_K}\right) + \frac{A_4}{A_6 + D} \sigma^{4.5} * EXP\left(-\frac{Q_2}{RT_K}\right) + A_7 f''' \sigma * EXP\left(-\frac{Q_3}{RT_K}\right), \quad (8)$$

where $\dot{\epsilon}$ is the creep rate tensor (-/s), σ is the Von Mises stress (Pa), T_K is the temperature (K), f''' is the fission rate density (fission/m³-s), G is the average grain diameter (μ m), R is the gas constant, and the other variables are given in the following.

$$\begin{aligned} A_1 &= 0.3919, \\ A_2 &= 1.31 \times 10^{-19}, \\ A_3 &= -87.7, \\ A_4 &= 2.0391 \times 10^{-25}, \\ A_6 &= -90.5, \\ A_7 &= 3.72264 \times 10^{-35}, \\ D &= \frac{\rho_0}{10980} 100, \\ Q_1 &= \frac{9000}{M} + 36294.4, \\ Q_2 &= \frac{10000}{M} + 56431.8, \\ Q_3 &= 2617, \\ M &= EXP\left[-\frac{20}{\log(OU_{ratio}-2)} - 8\right] + 1, \end{aligned} \quad (9)$$

where OU_{ratio} is the initial oxygen-to-uranium atom ratio. This property is not expected to play a significant role in the stresses of the structural materials because of the low burnup of the design.

However, UO₂ creep can be modeled if the fuel swelling is expected to induce noticeable strain in the surrounding materials.

2.1.4 Swelling

The swelling is given by Equation 10 (Allison 1993, Rashid 2004).

$$\begin{aligned}
 S &= ss + gs + den, \\
 ss &= 5.577 \times 10^{-5} \rho_0 B, \\
 gs &= \left[\frac{-1.96 \times 10^{-31}}{0.0178} \text{EXP}(-0.0178 \rho_0 B) + \frac{1.96 \times 10^{-31}}{0.0178} \right] (2800 - T_K)^{11.73} \text{EXP}[-0.0162(2800 - T_K)], \quad (10) \\
 den &= 0.01 \left[\exp\left(\frac{c_1}{c_{fact}}\right) - 1 \right], \\
 c_1 &= \frac{-4.60517 B_{mwd}}{5}, \\
 c_{fact} &= \begin{cases} 7.235 - 0.0086(T_C - 25) & \text{if } T_C < 750 \text{ }^\circ\text{C} \\ 1 & \text{if } T_C > 750 \text{ }^\circ\text{C} \end{cases}
 \end{aligned}$$

where S is the volumetric swelling (-), ss is the solid fission product swelling (-), gs is the gaseous fission product swelling (-), den is the densification (-), B is the burnup in FIMA, B_{mwd} is the burnup in (Megawatt Days per kilogram [MDW/kg]), and T_C is the temperature in degrees Celsius (°C). Figure 4 shows the UO₂ swelling versus burnup for three temperatures. For temperatures less than about 1,300K, the trend is dominated by the initial densification and subsequent solid fission product swelling terms. However, at higher temperatures the gaseous swelling term becomes significant, as shown in the 1,473K trend.

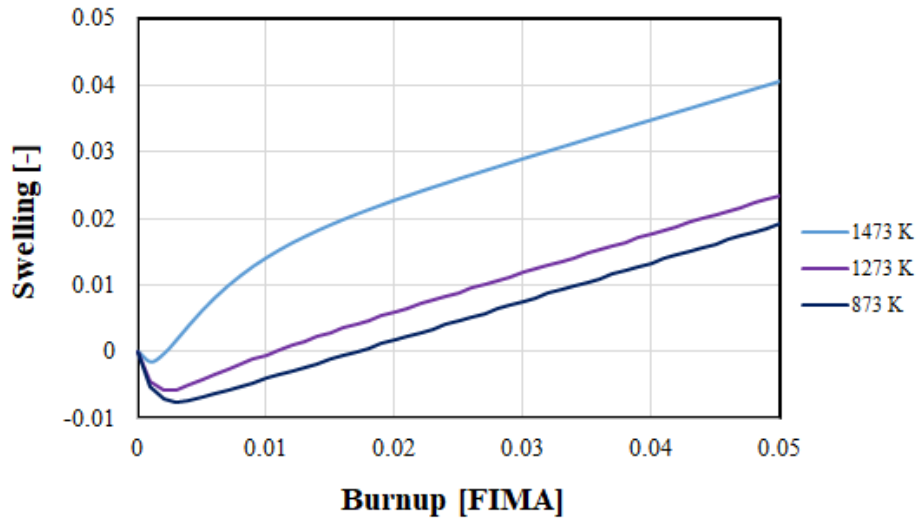


Figure 4. UO₂ swelling versus burnup and temperature.

2.1.5 Coefficient of Thermal Expansion

The coefficient of thermal expansion (CTE) was set to a constant 10⁻⁵. A MATPRO correlation does exist that could be implemented. However, for simplicity a constant value was used, and the default BISON value was selected. The stress-free temperature was set to 298K.

2.1.6 Initial Density

The initial density was set to $10,400\text{kg/m}^3$. The theoretical density was taken as $10,980\text{kg/m}^3$; $10,400$ is about 95% of the theoretical density (TD).

2.1.7 Elastic Properties

The elastic modulus was set to 200GPa , and Poisson's ratio was set to 0.345 . MATPRO correlations are available, but as before with the CTE, a default BISON value was selected for simplicity.

2.2 STAINLESS STEEL 316

2.2.1 Thermal Conductivity

The thermal conductivity for SS316L is given by Equation 11 (Mills 2002).

$$k = -7.301 \times 10^{-6} T_K^2 + 2.716 \times 10^{-2} T_K + 6.308, \quad (11)$$

where k is the thermal conductivity (W/m-K) and T_K is the temperature (K). Figure 5 shows the SS316L thermal conductivity versus temperature. The trend shows an increase in thermal conductivity with temperature until about $1,800\text{K}$.

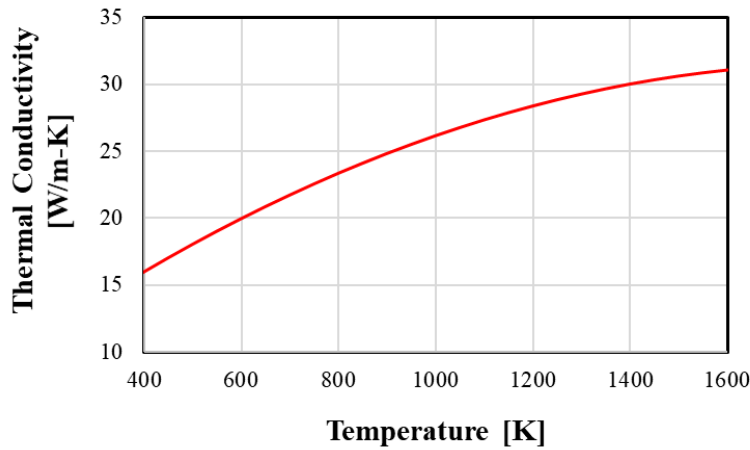


Figure 5. Plot of the SS316L thermal conductivity versus temperature.

2.2.2 Specific Heat

The specific heat is given by Equation 12 (Mills 2002).

$$c_p = 0.1816 T_K + 428.46, \quad (12)$$

where c_p is the specific heat (J/kg-K) and T_K is the temperature (K). Figure 6 shows the specific heat of the SS316L. The trend is a linear increase with temperature.

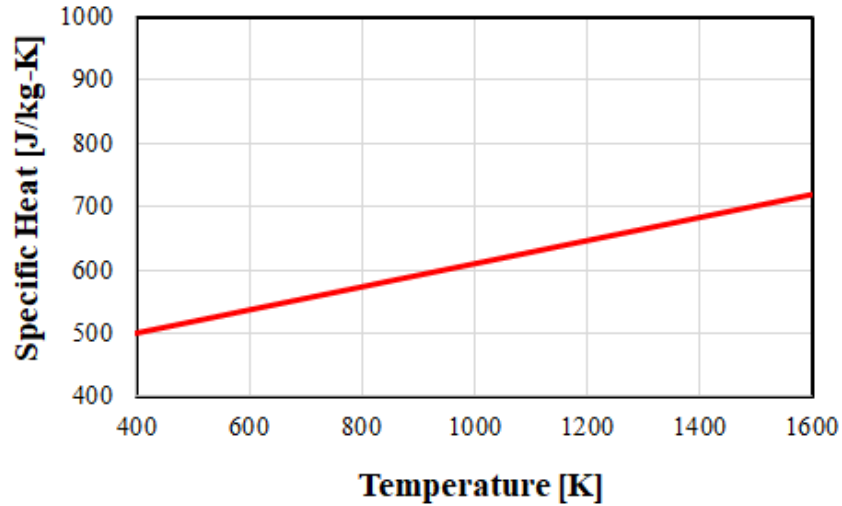


Figure 6. Plot of the SS316L specific heat versus temperature.

2.2.3 Coefficient of Thermal Expansion

The CTE for SS316L was set to a constant 18.7×10^{-6} . This is based on a table listed in Reference (United Performance Metals). The stress-free temperature was set to 298 K. There are sparsely tabulated values available, and a correlation could be fit to these values.

2.2.4 Initial Density

The initial density was set to a constant $7,800 \text{kg/m}^3$. This is an approximation of the density of SS316L. At this time, the density does not impact the other correlations for SS316L.

2.2.5 Plasticity

The yield stress of the SS316L is given by Equation 13. The values are based on a table published by Reference (Fahr 1973).

$$\sigma_y = \sigma_y^0 + K \varepsilon_p^n, \quad (13)$$

where σ_y is the yield stress (MPa), σ_y^0 (125 MPa) is the initial yield stress, K (500 MPa) is the hardening constant, n (0.4 -) is the hardening power, and ε_p is the plastic strain (-). Figure 7 plots the modeled yield stress of SS316L at 600°C. The yield stress would in practice be a function of temperature. However, the yield stress of the SS316L produced through additive manufacturing may be considerably different from the SS316L commonly produced by other processes.

A brief description of the plasticity model is as follows. When the Von Mises stress exceeds the yield stress by a user set fraction, the time step size is reduced and the plastic strain increment is calculated as the difference between the Von Mises stress and yield stress divided by the elastic modulus. This process continues until the Von Mises stress has been reduced to the yield stress and then simulation resumes its normal time steps.

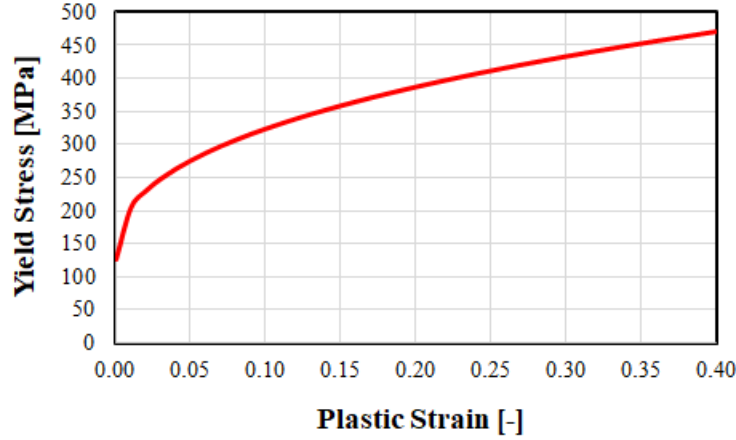


Figure 7. Plot of the SS316L yield stress versus plastic strain.

2.2.6 Elastic Properties

The elastic modulus was set to a constant 150GPa (British Stainless Steel Association). The modulus decreases with temperature, and an estimate of the value at 600°C was selected. The Poisson ratio was set to a constant 0.32 (British Stainless Steel Association).

2.3 SIC AND SIC WITH EMBEDDED TRISO

2.3.1 Thermal Conductivity

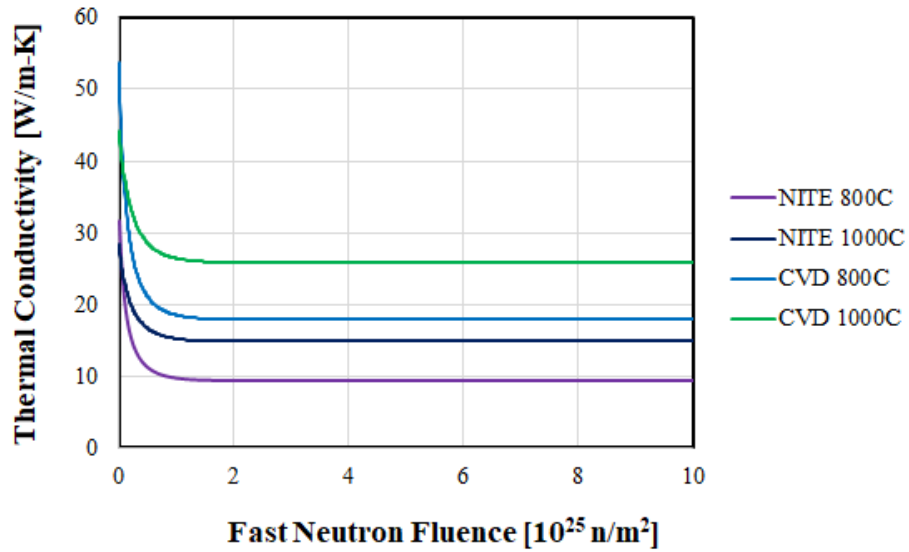
There are four thermal conductivity correlations for SiC in BISON, and additional correlations can be added or modified as needed. Equation 14 list these correlations.

$$\begin{aligned}
 k_{irrad} &= 6.7 \times 10^{-3} T_C + 4.22 , \\
 k_{unirrad} &= \frac{1}{3.28 \times 10^{-5} T_C + 3.5 \times 10^{-2}} , \\
 k_{nite} &= \frac{1}{(1.6498 \times 10^{-2} + 1.882 \times 10^{-5} T_C) + (2 * 5.2007 S)} , \\
 k_{cvd} &= \frac{1}{(2.68588 \times 10^{-3} + 1.993333 \times 10^{-5} T_C) + (5.2007 S)} ,
 \end{aligned} \tag{14}$$

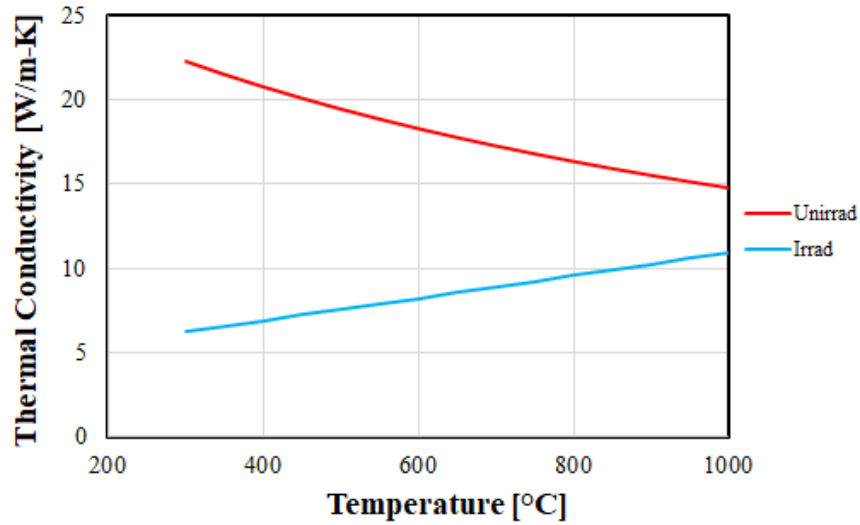
where k is the thermal conductivity (W/m-K), T_C is the temperature (°C).

Figure 8 plots the thermal conductivity equations. The unirradiated thermal conductivities of the Chemical Vapor Deposited (CVD) and Nano-Infiltrated Transient Eutectic (NITE) SiC correlations at 800°C are 53 and 31 W/m-K, respectively. The k_{nite} correlation was selected for the SiC can, and the k_{irrad} correlation was selected for the fueled SiC region. The k_{nite} includes the thermal conductivity degradation of the SiC with fast neutron fluence. The k_{irrad} correlation was selected for the fueled SiC region since the TRISO particles produce a noticeable thermal resistance that is present throughout the irradiation. Thus, approximating the thermal conductivity of the fueled region as independent of fluence and burnup seems appropriate as a first-order estimate. It is expected that the selection of these two correlations is a conservative choice and the real thermal conductivity is expected to be higher. However, owing to the parametric analysis approach, our findings provide a general overview of the trends that are not

unique to this choice. As experimental data on the thermal conductivity values emerge, they may simply be mapped across our parametric analysis.



(a)



(b)

Figure 8. Plots of the thermal conductivities for SiC versus temperature and fluence.

2.3.2 Specific Heat

The specific heat is given by Equation 15 (Snead 2007).

$$c_p = 925.65 + 0.3772T_K - 7.9259 \times 10^{-5} T_K^2 - \frac{3.1946 \times 10^7}{T_K^2}, \quad (15)$$

where c_p is the specific heat (J/kg-K) and T_K is the temperature (K). Figure 9 plots the SiC specific heat versus temperature. The trend is an increase with temperature.

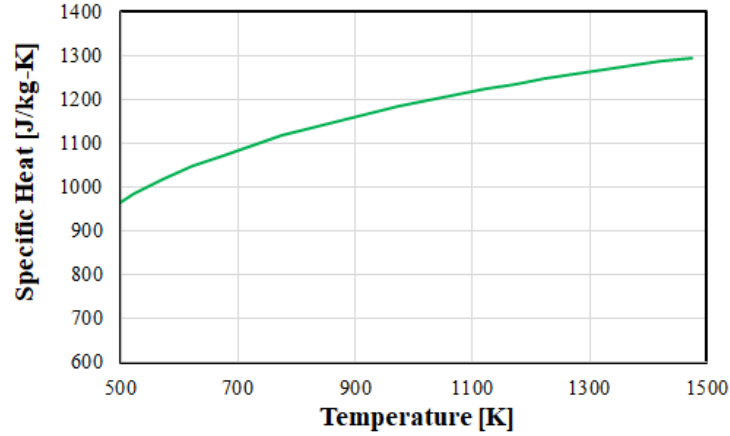


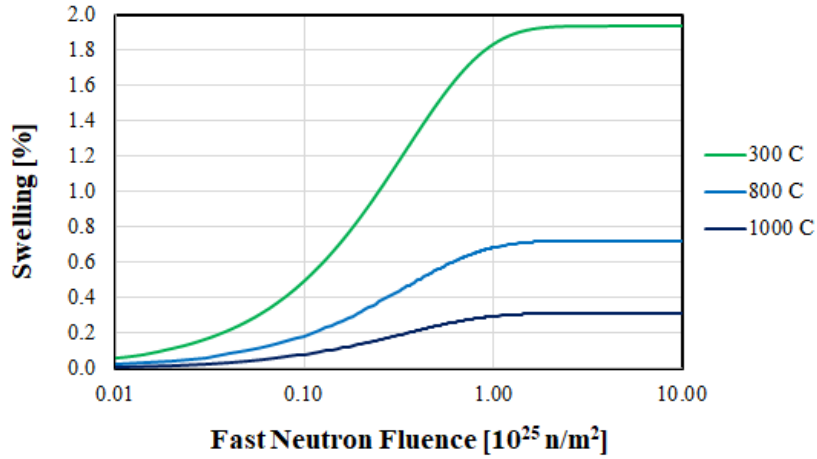
Figure 9. Plot of the SiC-specific heat versus temperature.

2.3.3 Swelling

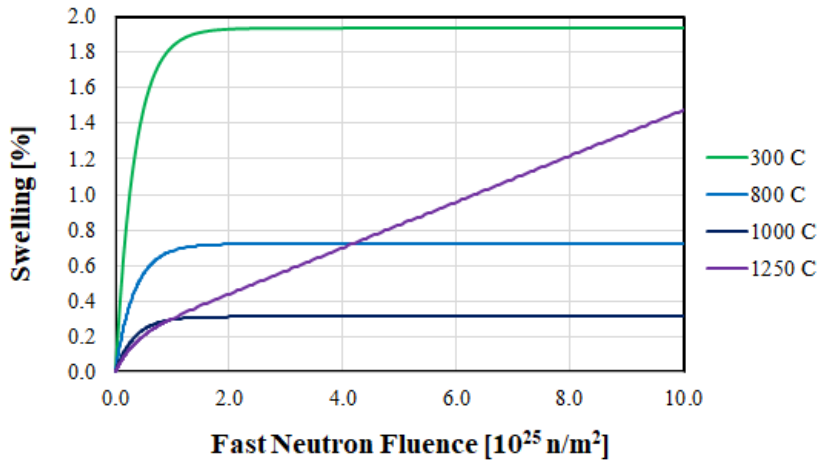
The swelling of the SiC is a piecewise function given in Equation 16 and based on data presented in (Ben-Belgacem 2014, Price 1977). The swelling is interpolated between the temperatures of 1,000°C and 1,250°C.

$$S = \begin{cases} (-2.43725 \times 10^{-3} T_C + 2.6702) \left[1 - \text{EXP} \left(-\frac{\Phi}{0.3396} \right) \right] & \text{if } T_C < 800 \text{ } ^\circ\text{C} \\ (-2.0505 \times 10^{-3} T_C + 2.3606) \left[1 - \text{EXP} \left(-\frac{\Phi}{0.3396} \right) \right] & \text{if } 800 \text{ } ^\circ\text{C} \leq T_C \leq 1000 \text{ } ^\circ\text{C}, \\ 0.18 \left[1 - \text{EXP} \left(-\frac{\Phi}{0.3396} \right) \right] + 0.1297 \Phi & \text{if } T_C > 1250 \text{ } ^\circ\text{C} \end{cases} \quad (16)$$

where S is the swelling (%), T_C is the temperature ($^\circ\text{C}$), and Φ is the fast neutron fluence ($E > 0.10 \text{ MeV}$) (10^{25} n/m^2). Figure 10 plots the SiC swelling. The lower temperatures swell sooner and saturate at larger values compared with the 1,000°C trend. However, the 1,250°C trend, which predicts cavity formation, follows a linear trend with fluence. Above 1,250°C, the model predicts a temperature-independent behavior.



(a)



(b)

Figure 10. Plots of the SiC swelling versus fluence and temperature. (a) Linear/log scale. (b) Linear/linear scale and the addition of the 1250 °C trend.

2.3.4 Coefficient of Thermal Expansion

The CTE for SiC is given by Equation 17 (Snead 2007).

$$CTE = -1.8276 + 0.0178T_K - 1.5544 \times 10^{-5}T_K^2 + 4.5246 \times 10^{-9}T_K^3, \quad (17)$$

where CTE is the coefficient of thermal expansion (10^6 -) and T_K is the temperature (K). The stress-free temperature was set to 298K. Figure 11 plots the CTE versus temperature. The trend follows an increase until about 900K.

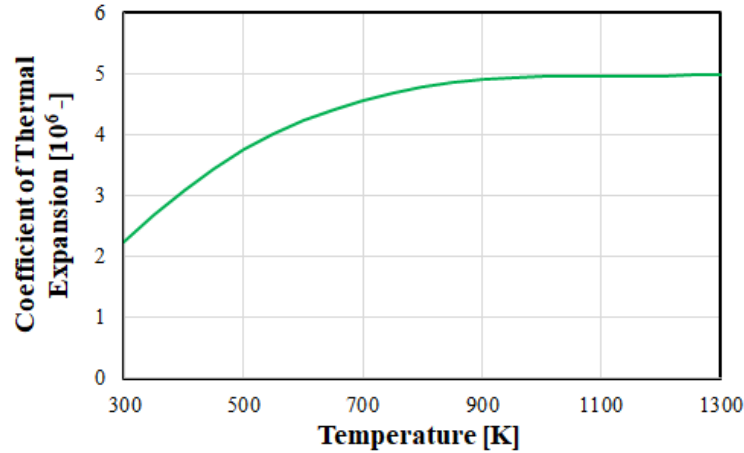


Figure 11. Plot of the SiC CTE.

2.3.5 Creep

The creep is given by Equation 18 (Ben-Belgacem 2014).

$$\dot{\epsilon} = K\sigma\dot{S}, \quad (18)$$

where $\dot{\epsilon}$ is the creep rate tensor (-/s), K is the creep constant ($0.55 \times 10^{-10} \text{ Pa}^{-1}$), σ is the stress tensor (Pa), and \dot{S} is the swelling rate (-). The creep of the SiC is on the order of 10^{-7} to 10^{-5} and is not expected to be significant to the analysis.

2.3.6 Initial Density

The initial density was set to $3,100 \text{ kg/m}^3$ for the SiC can and $2,700 \text{ kg/m}^3$ for the fuel-bearing SiC+TRISO material. At this time, the SiC correlations are not dependent on the density; however, it is expected that in practice the thermal conductivity and fracture parameters would depend on the density.

2.3.7 Elastic Properties

The elastic modulus was set to 400 GPa for the SiC can and 250 GPa for the fuel-bearing region. The Poisson ratio was set to 0.21.

3. METHODS

A simple geometry was selected for the sensitivity studies, which consisted of a small cylinder so that the computational requirements would be reasonable. The UO_2 geometry was an 11mm diameter, 8mm tall UO_2 cylinder, surrounded on three sides by a 1mm interface layer and a 1mm thick SS316L can. For the SiC simulations, the geometry was a 4mm tall, 13mm diameter fueled region surrounded on all sides by a 1mm SiC can. The total diameter was 15mm, and the total height was 6mm. A shorter pellet, compared with the UO_2 geometry, was used to prevent the location of the maximum stresses changing from the top and bottom along the centerline over to the side perimeter. With a taller pellet, the stresses would more often switch between the perimeter and axial centerline depending on the swelling and thermal expansion effects, which produced stress trends that were difficult to understand and unnecessarily complicated for the purposes of this report. For both the SiC and UO_2 geometries, the bottom outer curve of the can was constrained in the vertical axis using a Dirichlet boundary condition, while the top was allowed to move freely. The horizontal axes were constrained along their respective axes, which bisected the geometry. Figure 12 shows the simulated geometries. These geometries were selected because of their ability to show the effect of varying material properties without requiring expensive simulations. The elements were about 0.3mm on a side for a total of about 64,000 elements for the UO_2 geometry and 38,000 for the SiC geometry.

The power density was set to reach a maximum of $100\text{W}/\text{cm}^3$ in all simulations. The small distance between the centerline of the fuel and the coolant allowed for this power density without generating extreme stresses using nominal material properties. The UO_2 simulations were focused on the stresses included by thermal expansion. This focus was selected because of the maximum burnup being about 5% FIMA and because the CTE for the SS316L is greater than the UO_2 . Thus, the UO_2 simulations consisted of a ramp-up to full power over 10^4s .

The SiC simulations focused on both the stresses from thermal expansion and differential swelling. Thus, the SiC simulations consisted of a ramp to full power over 10^4s and subsequent operation at full power. The fluence at the end of the simulation reached $10^{25}\text{n}/\text{m}^2$, which is about the fluence for saturation of the low-temperature SiC swelling.

The third section of simulations focused on the effect of neglecting the fuel-free SiC shell and including the cavities for TRISO particles in the fueled SiC region. These simulations followed the other SiC simulations in a ramp to full power of $100\text{W}/\text{cm}^3$ and an end-of-simulation fluence of $10^{25}\text{n}/\text{m}^2$.

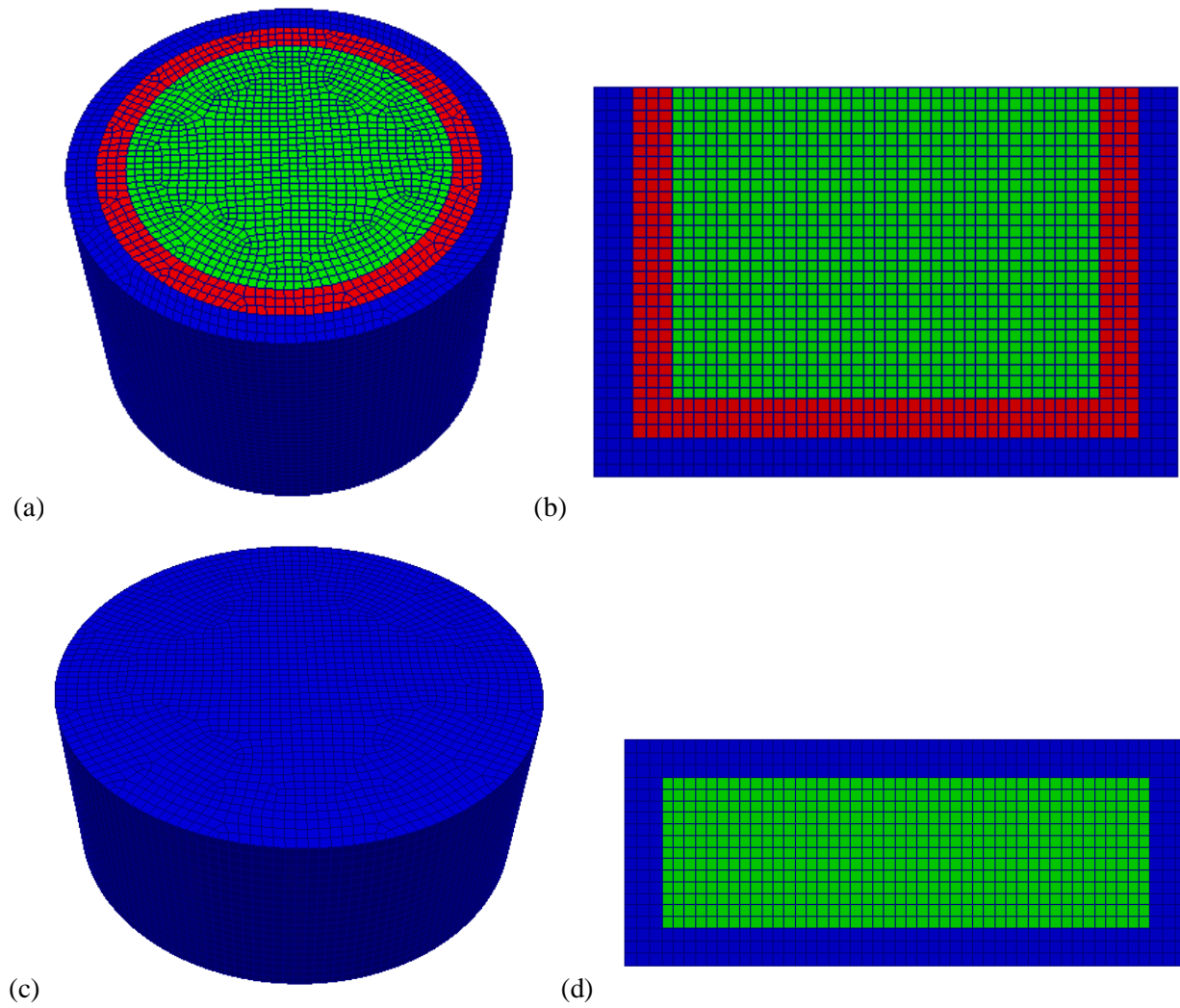


Figure 12. Representations of the meshes used for the sensitivity studies. Blue is the can, red is the interface layer, and green is the fuel. (a) UO_2 exterior view. (b) UO_2 cross section. (c) SiC exterior view. (d) SiC cross-section view.

4. RESULTS

The sensitivity studies were divided by material into four sections. These were the SiC shell, SiC fueled region, SS316L, and UO₂. The interface heat transfer coefficient variation is grouped with the SS316L simulations. The geometry and modeling method simulations are presented after the sensitivity study simulations.

The sampled material property values were selected for the purpose of investigating the:

- 1) Full range of possibilities. Such as the SiC can having a significantly larger CTE than the fueled region and vice versa.
- 2) Cover a sufficiently wide range so that a noticeable change in the stresses was predicted or the full range of possibilities were considered. This gives information on the extent to which the property must be varied before there is a significant effect.
- 3) Select a range wide enough so that the changes to the stress trends would be found. This is to ensure that if the model predicts very unexpected behavior, it will be known before hand as either a regime to avoid or a weakness in the model.
- 4) Simultaneous variations in multiple properties were not considered since it is difficult to determine the cause of the predicted trend with a high degree of confidence.

4.1 SIC CAN VARIATIONS

The general stress trends in the SiC concept are initially driven by the differential thermal expansion due to heat generation. Then the stresses usually decrease as the colder can swells to larger values than the fuel. Also, the onset of SiC swelling is modeled as occurring slightly earlier at lower temperatures. This earlier and larger swelling of the can compared with the fueled interior counteracts the larger thermal expansion of the fueled region. However, as the swelling continues, the swelling difference between the can and the fueled region usually exceeds the difference between their thermal expansions and the can is placed in compression and the stresses begin to climb.

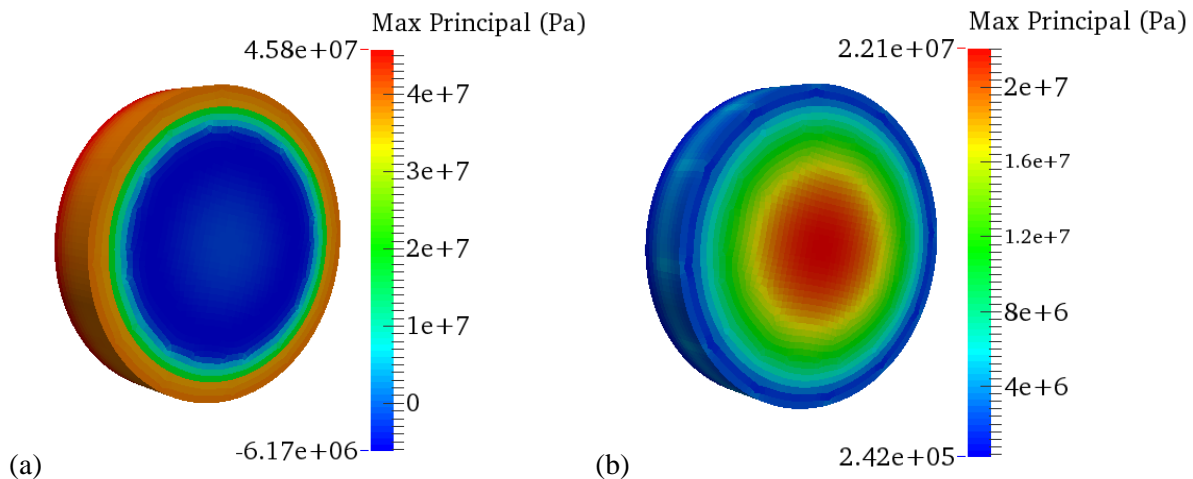


Figure 13. Maximum principal stress profiles in the SiC sensitivity study geometry using nominal values. (a) Thermal stresses after the power ramp. (b) Mostly swelling stresses at the saturation of the swelling.

4.1.1 Thermal Conductivity

The thermal conductivity of the can was multiplied by factors ranging from 0.5 to 10, while the thermal conductivity in the fueled region remained at its nominal values. Figure 14 shows the results. The initial stresses were due to the differential thermal expansion between the centerline and the perimeter. Thus, increasing the thermal resistance increased the centerline temperature and the initial stresses due to thermal expansion. The stresses then decreased as the greater swelling of the colder SiC can, which accommodated the larger thermal expansion of the fueled region. After reaching a minimum, the stresses began to climb due to the additional swelling of the colder can compared with the hotter fueled region. The thermal conductivity of the can noticeably affected the thermal expansion stresses in the can but had a fairly minor effect on the saturated swelling stresses in the can. However, both thermal expansion and swelling stresses in the fueled region varied noticeably as a result of the can thermal conductivity.

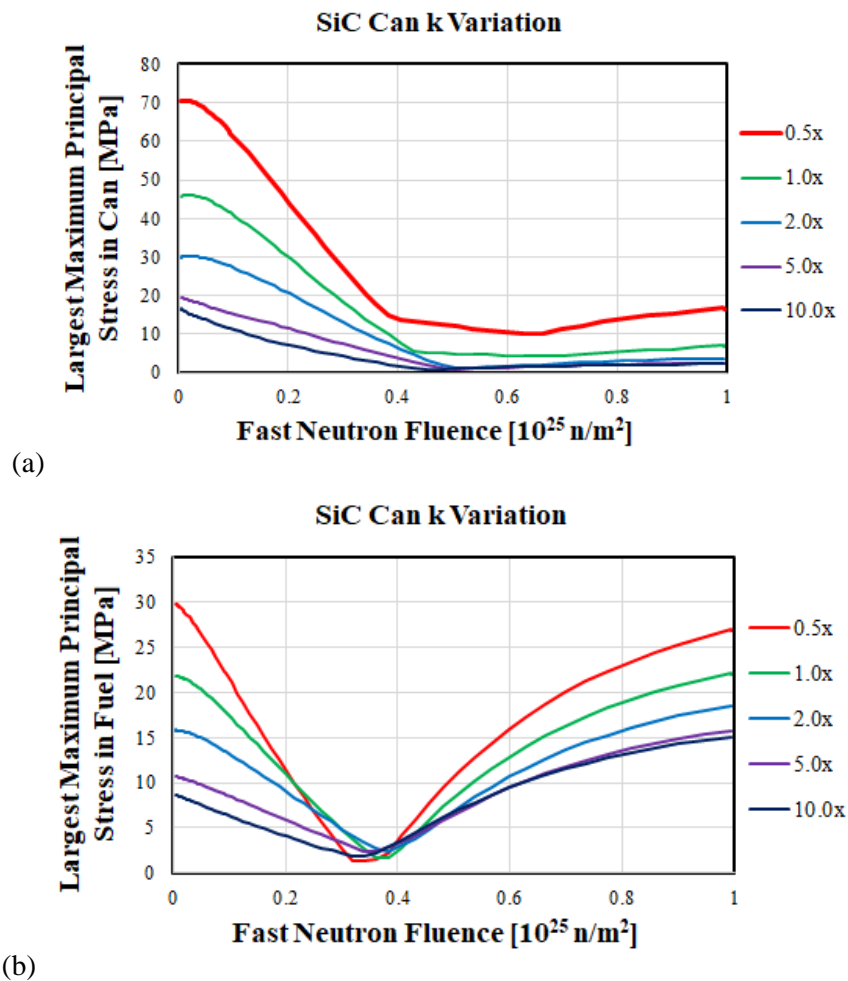


Figure 14. Largest maximum principal stress as a result of varying the thermal conductivity in the can. (a) Maximum principal stress in the can. (b) Maximum principal stress in the fueled region.

4.1.2 Coefficient of Thermal Expansion

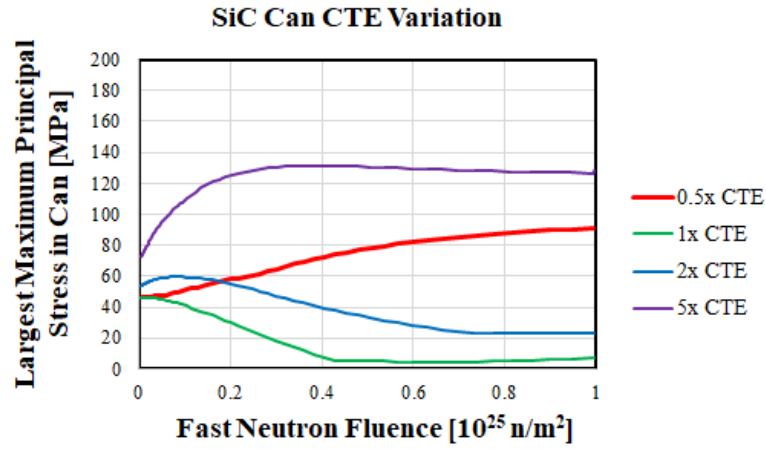
The CTE in the SiC can was multiplied by factors ranging from 0.5 to 5, while the CTE in the fueled region was unchanged. The results are plotted in Figure 15. The temperature along the centerline was somewhat hotter in the fuel compared with the can. As a result, when the CTE in the can was reduced to 0.5× its nominal value, the difference in swelling between the can and the fuel along the centerline was insufficient to compensate for the thermal expansion of the fuel in the vertical direction. As a result, the location of the maximum principal stress for this simulation was in the can along the centerline, and the stresses increased as the thermal conductivity degraded and the centerline temperature increased.

In the simulation where the CTE in the can was multiplied by a factor of 5, the thermal expansion of the can was sufficiently large that the additional swelling increased the maximum stress in the corners of the can. Then the thermal conductivity degradation increased the thermal expansion of the fuel and slightly reduced the stresses in the can. However, in the fuel, the maximum principal stress for the 5× case was located on the centerline top and bottom surfaces, and the stress in the fuel continued to increase due to thermal degradation and the higher CTE of the can.

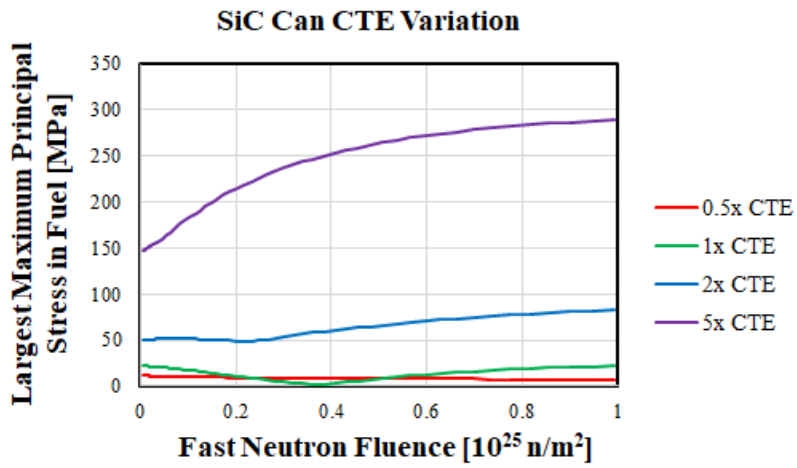
However, in the other two simulations where the CTE in the can was more comparable with the CTE of the fuel, the stress profile was reasonably typical in that the fuel thermal expansion initially induced stress in the can, which is subsequently compensated for by the can's larger swelling and stresses reached a minimum. Then as the swelling continued, the stresses slowly built up.

4.1.3 Elastic Modulus

The elastic modulus of the can was varied from 250 to 500GPa, and its nominal value was 400GPa. Figure 16 plots the results. The results show that the stresses in the can were proportional to the elastic modulus. However, in the fueled region the thermal expansion stresses decreased with the increasing elastic modulus of the can, while the reverse is true for the swelling stresses at the end of the simulation. The larger elastic modulus of the can resisted the displacement of the fueled region. After the power ramp, the can acted to compress the fueled region and a larger elastic modulus increased this effect; while at the end of the simulation, the can pulled the fueled region into tension and a larger elastic modulus increased this effect.

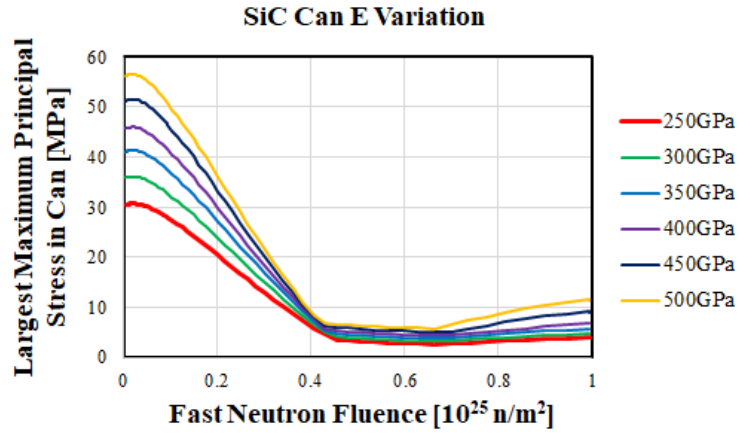


(a)

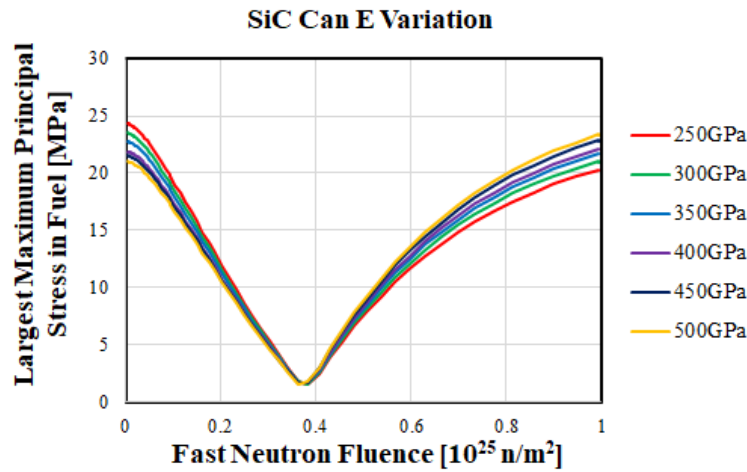


(b)

Figure 15. Largest maximum principal stress as a result of varying the CTE in the can. (a) Maximum principal stress in the can. (b) Maximum principal stress in the fueled region.



(a)

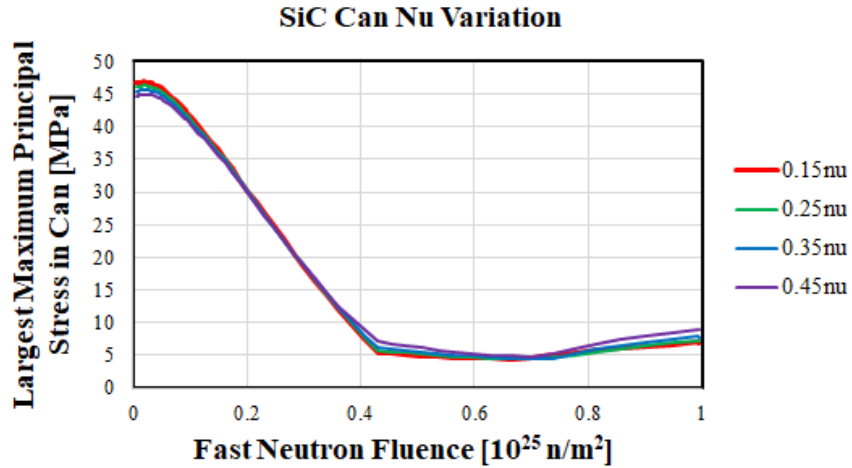


(b)

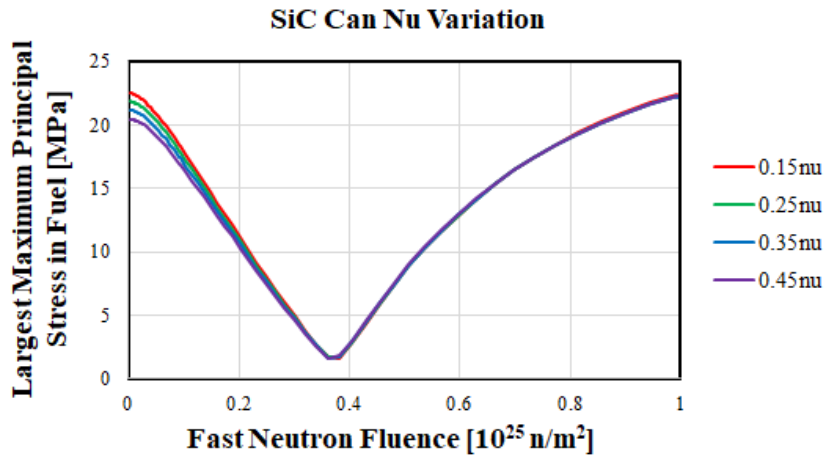
Figure 16. Largest maximum principal stress as a result of varying the elastic modulus in the can. (a) Maximum principal stress in the can. (b) Maximum principal stress in the fueled region.

4.1.4 Poisson's Ratio

Poisson's ratio in the SiC can was varied from 0.15 to 0.45. Figure 17 plots the results. The stresses showed minimal change due to the Poisson's ratio; therefore, the Poisson's ratio of the can does not appear to significantly affect the stresses in the SiC concept.



(a)

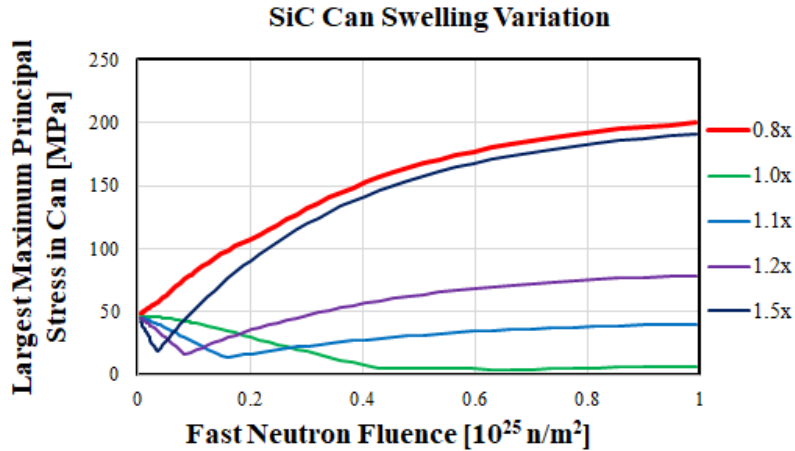


(b)

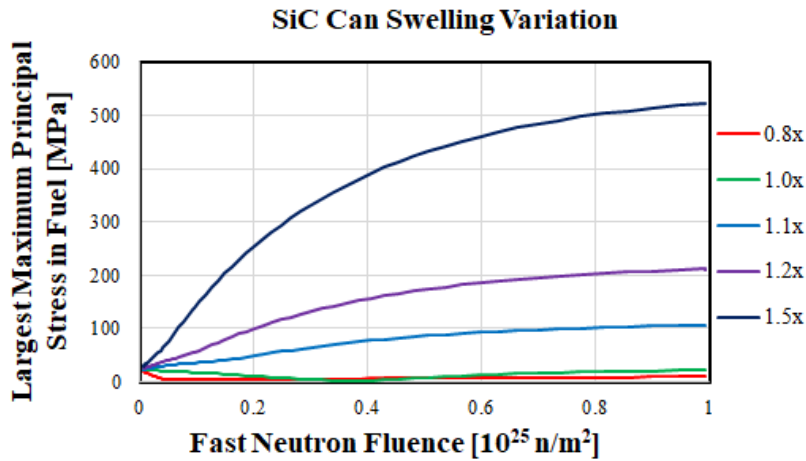
Figure 17. Largest maximum principal stress as a result of varying the Poisson's ratio in the can. (a) Maximum principal stress in the can. (b) Maximum principal stress in the fueled region.

4.1.5 Swelling

The swelling of the SiC can was varied from 0.8 to 1.5, and Figure 18 plots the resulting maximum principal stresses. In the 0.8× case, both the swelling and thermal expansion of the fuel were greater than the can. As a result, the fuel increasingly pushed against the can throughout the simulation, resulting in a continuously increasing maximum stress in the can. However, the stress in the fuel was compressive, and the maximum tensile stress was close to zero for the 0.8× case. As the swelling factor in the can exceeded that of the fuel, however, the fluence at which the stress minimum is reached was reduced, but the amount of swelling required to compensate for the higher thermal expansion of the fuel remained about the same. The subsequent increase in maximum stress following the minimum was proportional to the additional swelling in the can that was not needed to accommodate the thermal expansion in the fuel. The stresses in the can were increasingly tensile since the can was pulled outward by the larger swelling.



(a)



(b)

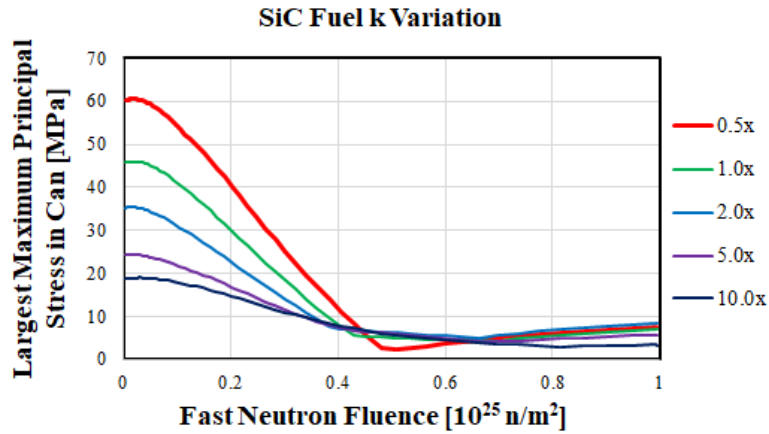
Figure 18. Largest maximum principal stress as a result of varying the irradiation swelling in the can. (a) Maximum principal stress in the can. (b) Maximum principal stress in the fueled region.

4.2 SIC-FUELED MATERIAL VARIATIONS

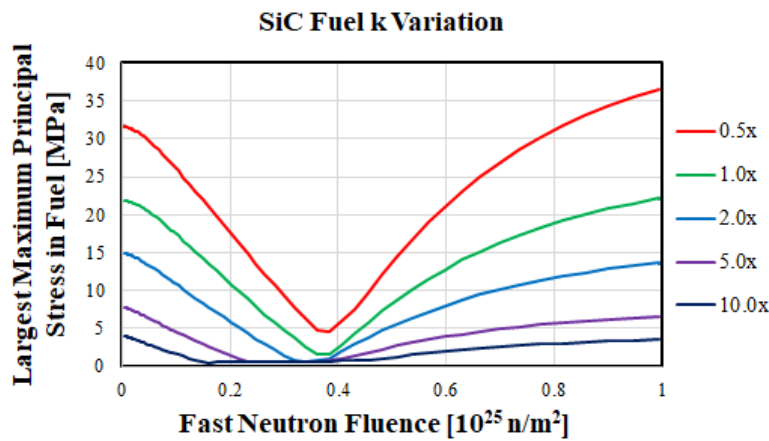
The difference between the following simulations and the previous simulations is that the material properties are being varied in the fueled region while the can maintains its nominal values.

4.2.1 Thermal Conductivity

The thermal conductivity of the fueled region was multiplied by factors ranging from 0.5 to 10, and the results are plotted in Figure 19. The stresses were similar to those predicted in the can thermal conductivity variation. The thermal expansion stresses in both the can and the fuel were inversely proportional to the fuel thermal conductivity. However, the swelling stresses in the can were largely unaffected by the fuel thermal conductivity, while the stresses in the fuel were strongly dependent on the fuel's thermal conductivity. The swelling stress dependence of the fueled region is due to the increasing thermal conductivity, which reduces the fuel's centerline temperature and reduces the difference between the swelling of the fuel and the can.



(a)

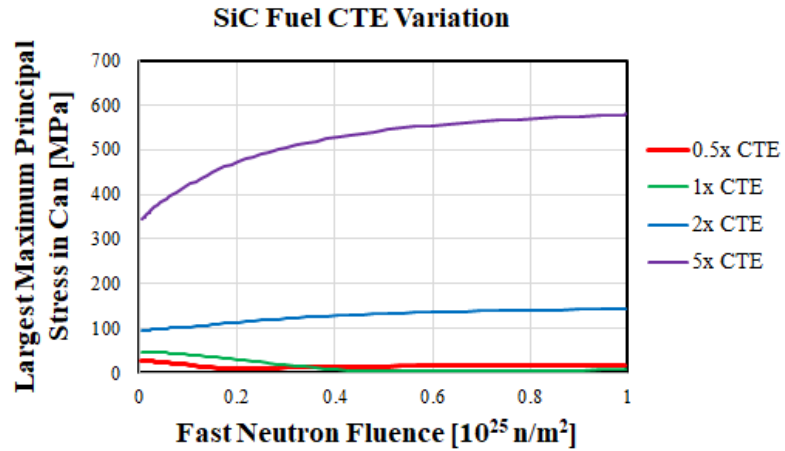


(b)

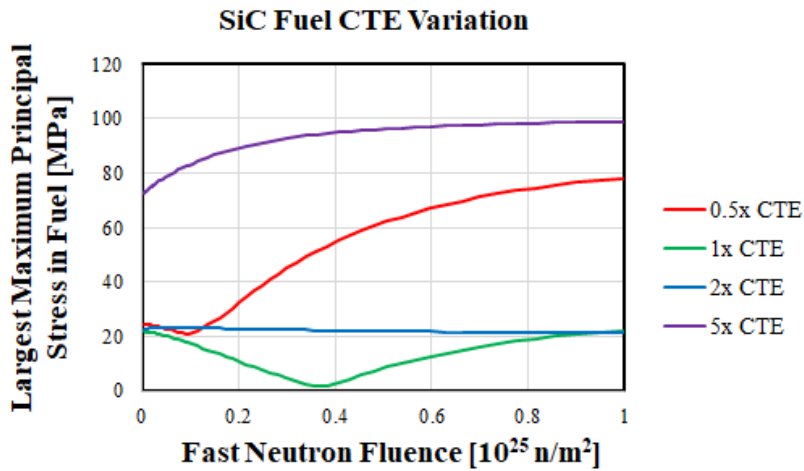
Figure 19. Largest maximum principal stress as a result of varying the thermal conductivity in the fueled region. (a) Maximum principal stress in the can. (b) Maximum principal stress in the fueled region.

4.2.2 Coefficient of Thermal Expansion

The CTE of the fuel was multiplied by factors ranging from 0.5 to 5, and the results are plotted in Figure 20. In the 0.5× case, the swelling of the can quickly accommodated the thermal expansion of the fuel and then pulled the fuel increasingly into tension. The 2× CTE case in the fuel was a unique condition where the thermal expansion of the fuel only somewhat overcompensated for the larger swelling in the fuel. The maximum stresses in the can were located on the centerline and increased slowly throughout the simulation. The stress in the fuel slowly decreased during the simulation as the can compressed the fuel. In the 5× case, the fuel increasingly pressed against the can, and the stresses in the can increased. The stresses also increased in the fuel at the corners because of the differential thermal expansion within the fuel. The hoop, radial, and axial stresses in the fuel remained compressive, but the maximum principal stress, which involved rotating the stress tensor so that the shear stresses were zero, continued to increase during the simulation.



(a)

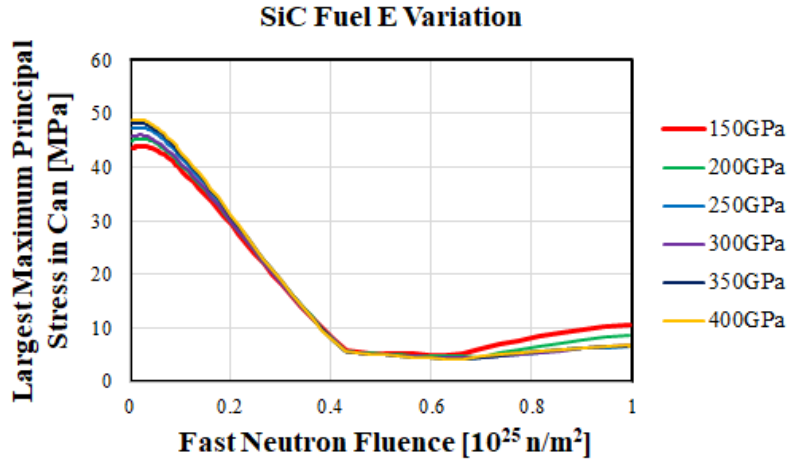


(b)

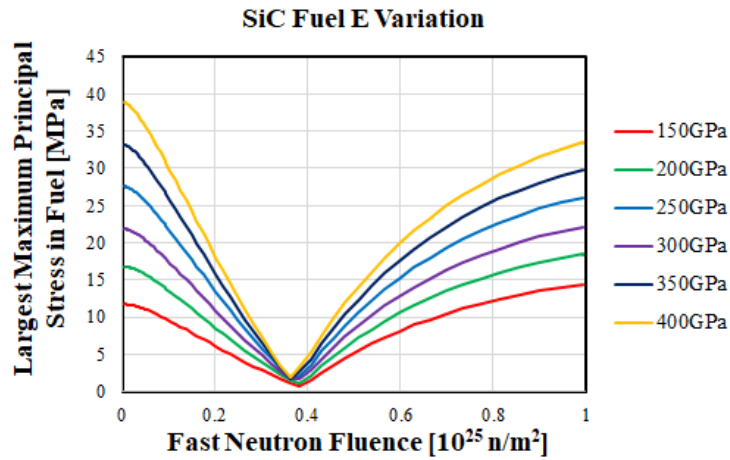
Figure 20. Largest maximum principal stress as a result of varying the CTE in the fueled region. (a) Maximum principal stress in the can. (b) Maximum principal stress in the fueled region.

4.2.3 Elastic Modulus

The elastic modulus of the fueled region was varied from 150 to 400GPa, and its nominal value was 250GPa. The results are plotted in Figure 21. The stresses in the can showed minor changes as a result of the variation in the elastic modulus of the fueled region. The thermal expansion stresses in the can increased slightly with fuel elastic modulus, and the swelling stresses decreased slightly with the fuel elastic modulus. However, the stresses in the fueled region were noticeably affected by and proportional to their elastic modulus.



(a)

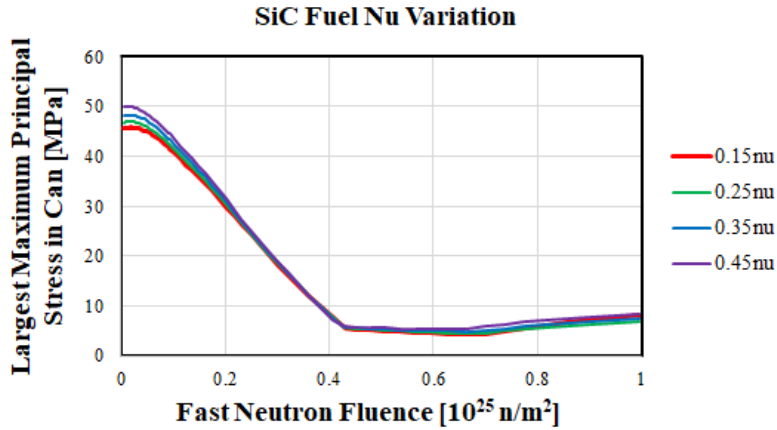


(b)

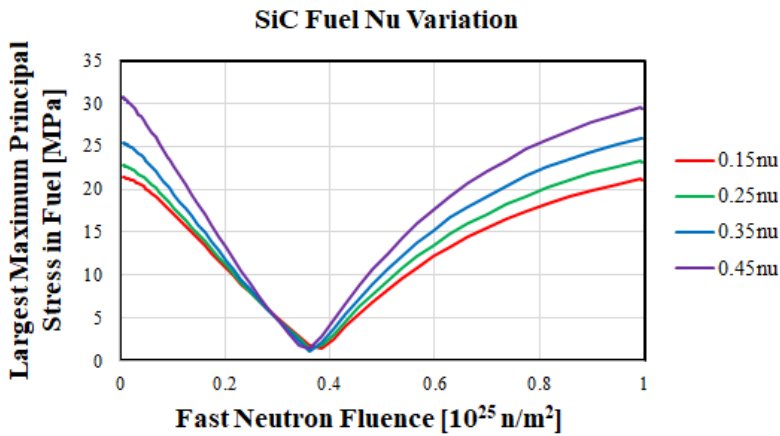
Figure 21. Largest maximum principal stress as a result of varying the elastic modulus in the fueled region. (a) Maximum principal stress in the can. (b) Maximum principal stress in the fueled region.

4.2.4 Poisson's Ratio

Poisson's ratio in the fueled region was varied from 0.15 to 0.45, and the results are plotted in Figure 22. The resulting stresses in the can showed minimal change, although there was some dependence in the fueled region. Poisson's ratio affected the volume change of the fueled region due to induced strain. When coupled the can that both surrounded and constrained the fueled region, some change in the stress was predicted due to this property. However, other properties produce larger variations compared with Poisson's ratio of the fueled region.



(a)



(b)

Figure 22. Largest maximum principal stress as a result of varying Poisson's ratio in the fueled region. (a) Maximum principal stress in the can. (b) Maximum principal stress in the fueled region.

4.2.5 Swelling

The swelling of the fueled region was multiplied by factors ranging from 0.8 to 1.5, and the results are plotted in Figure 23. The stress in can for the 1.1 \times , 1.2 \times , and 1.5 \times swelling cases continued to increase during the simulation as the fuel pressed against the can because of the larger swelling and thermal expansion strains. The stresses in the fuel for these cases was correspondingly small, which was expected.

In the 0.8 \times case, the stress in the fuel increased as it was pulled outward by the can. The largest maximum principal stress in the can was located at the inside corners, and the radial and axial stresses were tensile at these locations. These stresses continued to increase the swelling mismatch between the fuel and the can.

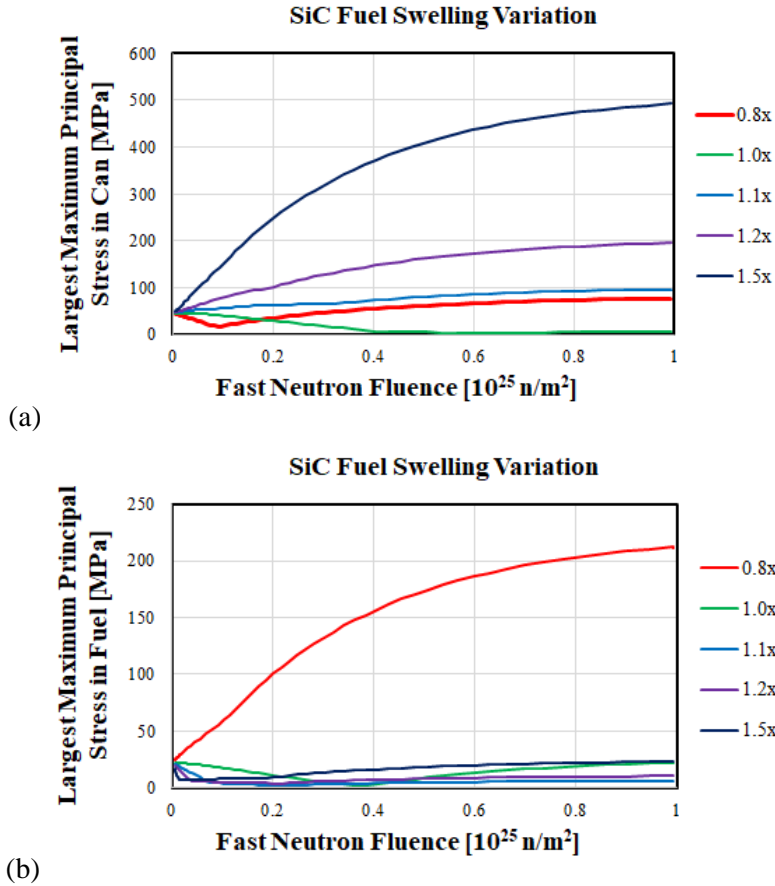


Figure 23. Largest maximum principal stress as a result of varying Poisson's ratio in the fueled region. (a) Maximum principal stress in the can. (b) Maximum principal stress in the fueled region.

4.3 STAINLESS STEEL 316L

These simulations focused on the UO_2 fuel in the SS316L cans with a bristle interface layer between the stainless steel and the UO_2 . Because fuel swelling could be accommodated by the interface layer's ability to plastically deform, these simulations focused on the thermal expansion stresses due to a power ramp. The CTE for SS316L is larger than UO_2 , and as a result the stresses in the SS316L can are caused by its own temperature profile. The power was ramped to $100\text{W}/\text{cm}^3$ over $1 \times 10^4\text{s}$. The interface layer was 1 mm thick and was given a thermal conductivity of $0.8\text{W}/\text{m}\cdot\text{K}$, which is equivalent to a heat transfer coefficient of $800\text{W}/\text{m}^2\cdot\text{K}$ (based on early experimental measurements on the nonoptimized 3D printed bristle wall builds under the TCR program). The elastic modulus of the interface was set to 1kPa to allow the SS316L can to expand away from the fuel since they are not bonded together. Figure 24 shows the temperature and stress profiles in the SS316L can at $100\text{W}/\text{cm}^3$.

The temperature of the SS316L can is hottest in the center of the bottom plate because of its proximity to the centerline of the fuel. This causes larger thermal expansion in the bottom of the can compared with the sides. As a result, the largest tensile stresses are in the bottom corners of the can and the largest compressive stresses are on the top surface at the center of the can's bottom plate.

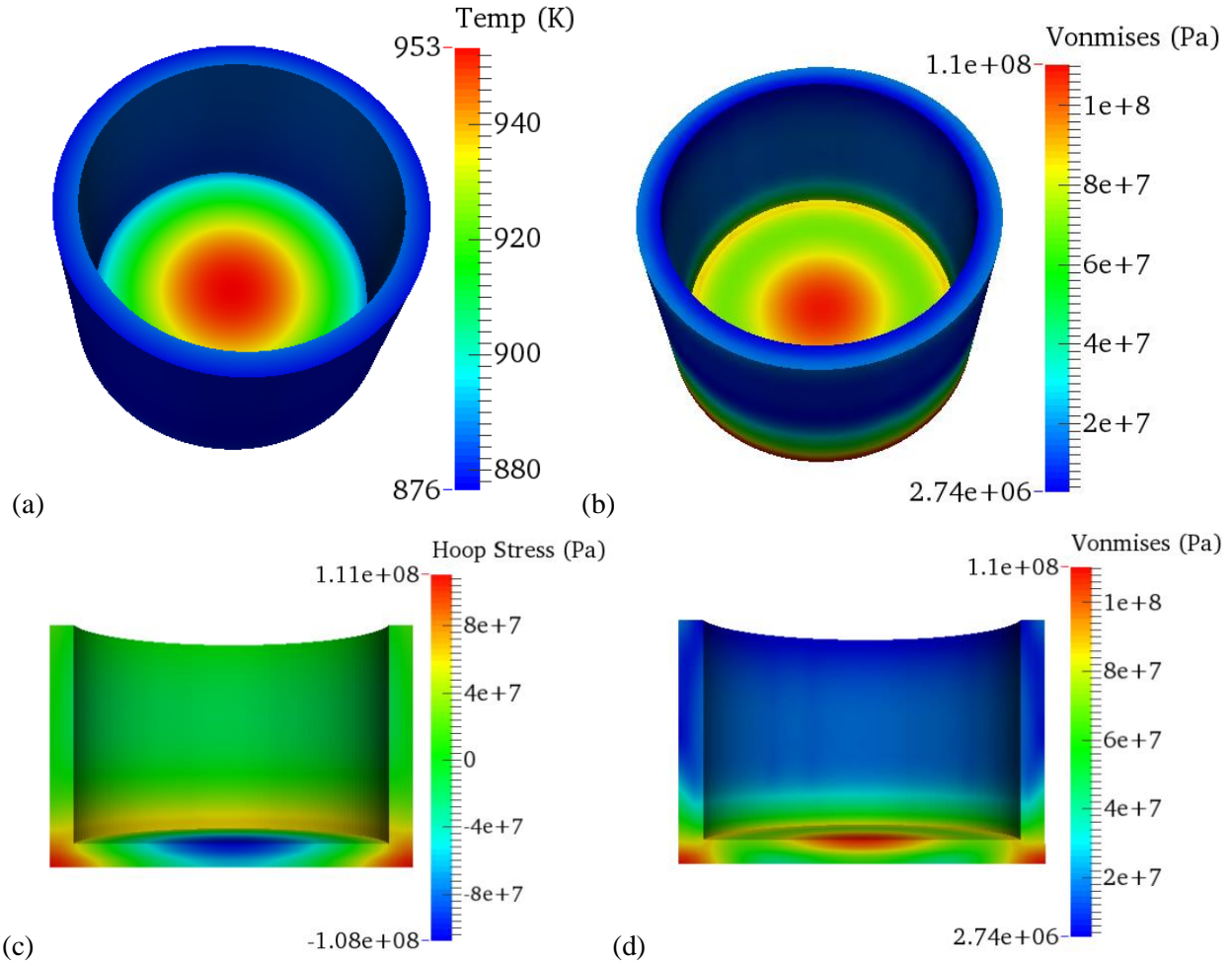
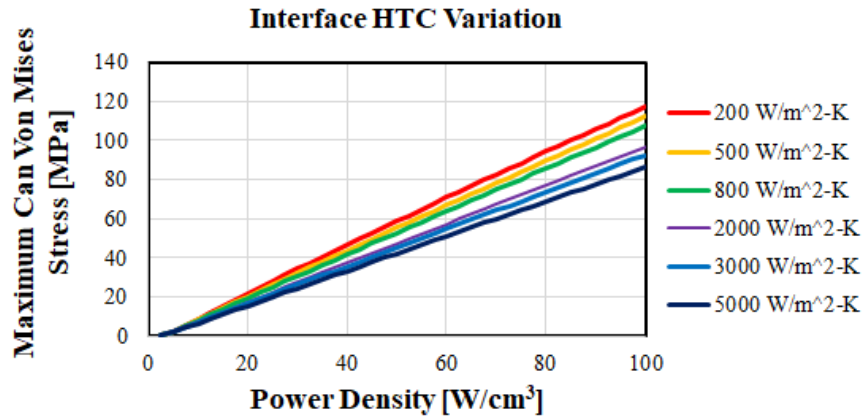


Figure 24. Temperature and stress profile in the SS316L can as a result of thermal expansion at 100 W/cm^3 . (a) Temperature profile. (b) Von Mises stress profile. (c) Hoop stress cross section. (d) Von Mises stress cross section.

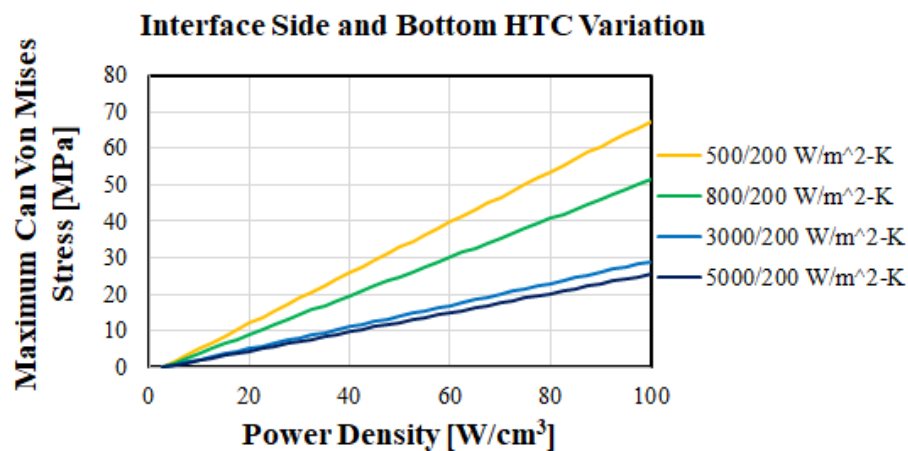
4.3.1 Interface Heat Transfer Coefficient

The thermal conductivity of the interface layer was varied from 0.2 to 5 W/m-K . Since the interface layer is 1 mm thick this is equivalent to a heat transfer coefficient (HTC) of 200 to $5,000 \text{ W/m}^2\text{-K}$; the nominal value is $800 \text{ W/m}^2\text{-K}$. Figure 25a plots the resulting maximum Von Mises stress in the can as a result of varying the interface HTC on all sides. However, Figure 25b plots the maximum Von Mises stress in the can as a result of varying the side interface layer HTC from 500 to $5,000 \text{ W/m}^2\text{-K}$ while the bottom layer is held at $200 \text{ W/m}^2\text{-K}$. This effectively tested the effect of the ratio of side to bottom HTCs.

The stresses in the can are inversely proportional to the interface HTC since this increases the fuel centerline temperature and the thermal expansion in the center of the can's bottom plate. However, it was noticed that the stresses were reduced when the HTC of the bottom interface was reduced to $200 \text{ W/m}^2\text{-K}$. Reducing this HTC reduced the heat flow into the bottom of the can and correspondingly its maximum temperature, which affected the thermal expansion strain.



(a)



(b)

Figure 25. (a) Maximum Von Mises stress in the SS316L can as a result of varying the interface HTC. (b) Maximum Von Mises stress in the SS316L can as a result of varying the side interface HTC while the bottom surface was held at 200W/m²-K.

4.3.2 Thermal Conductivity

The thermal conductivity of the SS316L can was multiplied by factors ranging from 0.1 to 100, and Figure 26 shows the results. The stresses were significantly dependent on the thermal conductivity of the can. However, it is acknowledged that the thermal conductivity of SS316L is highly unlikely to reach values of 2 or 2000W/m-K. However, the results show a high degree of sensitivity in the 0.2 to 2× range.

As the thermal resistance increased, the fuel centerline increased as did the temperature of the bottom plate of the can, resulting in larger thermal expansion stresses. The difference between these simulations and the previous interface thermal conductivity simulations is that while both involve increasing the thermal resistance, in these simulations the heat flow was reduced at the inner can interface. Thus, the inside of the can experienced high temperatures of about 1,230K in the 0.1× case compared with 950K in the 1× case.



Figure 26. Plot of the maximum Von Mises stress in the SS316L can as a result of varying the SS316L thermal conductivity.

4.3.3 Coefficient of Thermal Expansion

The CTE of the SS316L can was varied from 10 to 30×10^{-6} , and Figure 27 plots the results. As expected, the stress in the can was proportional to its thermal expansion. The larger CTE increased the amount of thermal expansion that the perimeter restrains, and the stresses increased correspondingly.

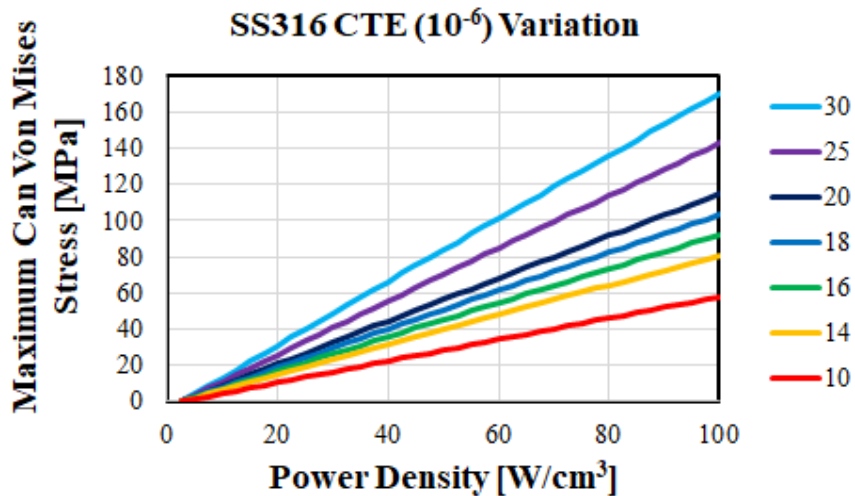


Figure 27. Plot of the maximum Von Mises stress in the SS316L can as a result of varying the SS316L CTE.

4.3.4 Elastic Modulus

The elastic modulus of the SS316L can was varied from 50 to 300GPa, with its nominal value being 190GPa. The results are plotted in Figure 28. The stresses in the can followed the ratio of the elastic moduli. Since the strains are reasonably constant, the stresses must increase accordingly with the elastic modulus.

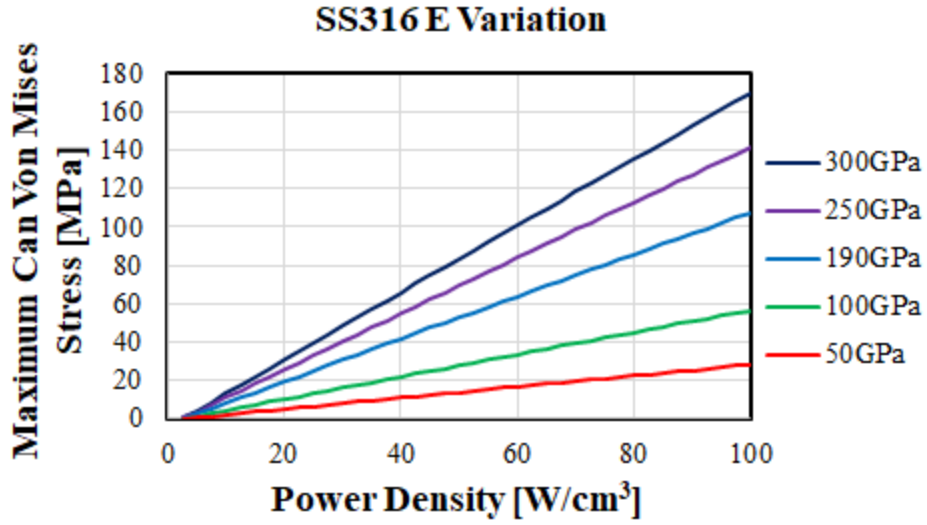


Figure 28. Plot of the maximum Von Mises stress in the SS316L can due to varying the elastic modulus.

4.3.5 Poisson's Ratio

The Poisson's ratio of the SS316L can was varied from 0.15 to 0.45 with a nominal value of 0.265, and the results are plotted in Figure 29. The results show a small increase in the stresses within the can. However, this effect is minor compared with the other properties.

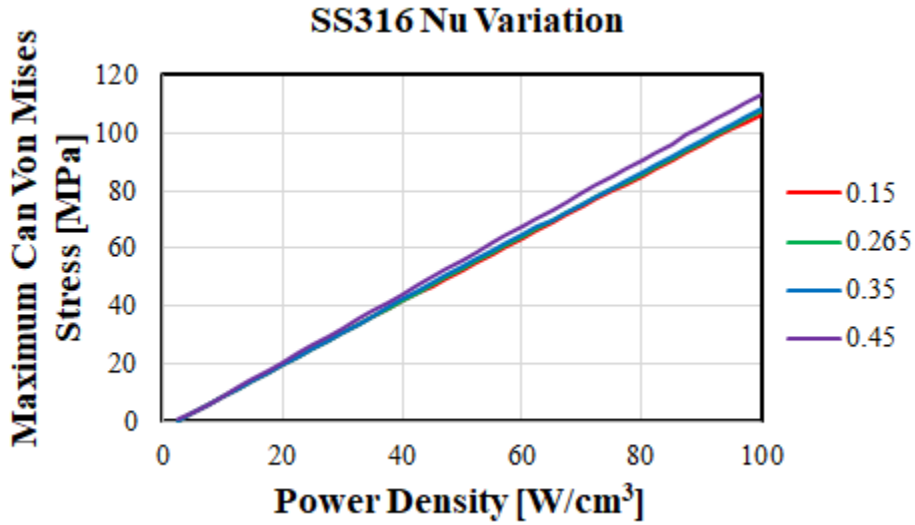


Figure 29. Plot of the maximum Von Mises stress in the SS316L can due to varying Poisson's ratio.

4.4 URANIUM DIOXIDE

4.4.1 Thermal Conductivity

The thermal conductivity of UO_2 was multiplied by factors ranging from 0.2 to 100. The results are plotted in Figure 30. The results indicate that the thermal conductivity of the UO_2 had essentially no impact on the stresses in the can. This is because the fuel is not pressing up against the can. However, in geometries where the expansion of the fuel is the primary stress driver in the can/cladding, the thermal conductivity of the fuel would have a more important effect.

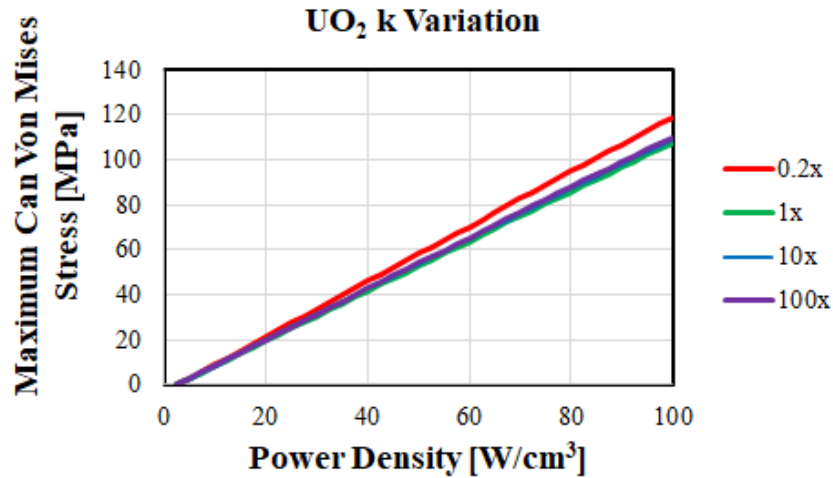


Figure 30. Plot of the maximum Von Mises stress in the SS316L can due to varying the UO_2 thermal conductivity.

4.5 GEOMETRY AND MODELING METHODS

4.5.1 Silicon Carbide Can

The effect of simulating the SiC plus TRISO-fueled region and the SiC can as a single volume was considered. For these simulations, a “Y” shaped geometry was used, as shown in Figure 31. The can layer was 2mm thick on all sides, the total height was 22mm, and the length of a flat side was 29mm. In all simulations the same geometry was used. However, the simulations with one set of properties used a mesh, with all of the volumes placed in the same block rather than being separated into their respective can and fuel blocks.

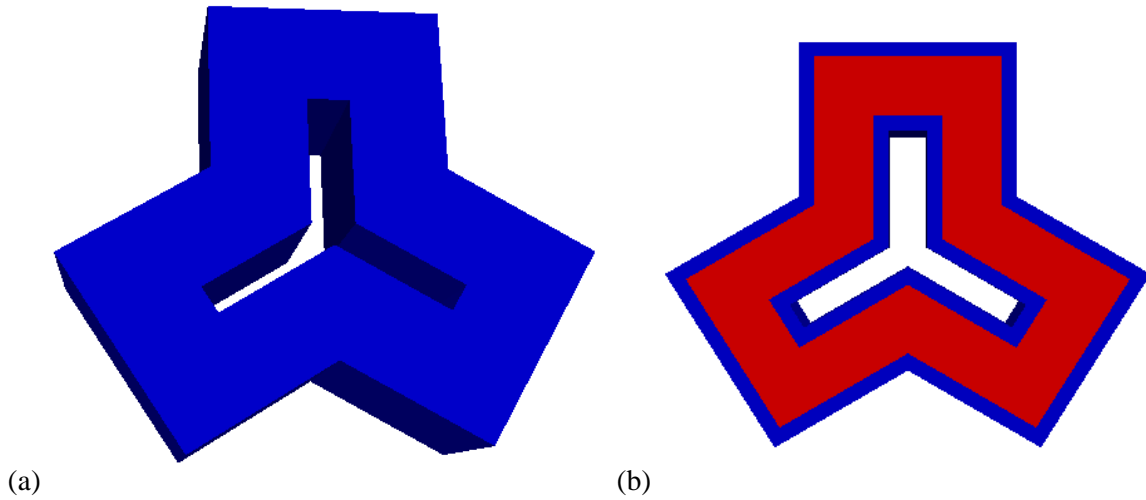


Figure 31. Y mesh geometries used for estimating the effect of completely homogenizing the SiC geometries. (a) Outer view. (b) Cross section view.

Four simulations were performed. The first operated at $50\text{W}/\text{cm}^3$ in the fueled region and without heat generation in the can to a total heat production of (1,141.55W). Nominal material properties were used for the can and fueled regions, which have different thermal conductivities and elastic moduli. The second simulation operated at $50\text{W}/\text{cm}^3$ in the fueled region, also without heat generation in the can, but with the same properties in the can and fueled region. The thermal conductivity in this simulation and the two subsequent simulations were set to Equation 19:

$$k_{irrad} = 6.7 \times 10^{-3} T_C + 4.22 , \quad (19)$$

where T_C is the temperature in ($^{\circ}\text{C}$). The elastic modulus was set to 250GPa. The third simulation operated at $50\text{W}/\text{cm}^3$ in both the fueled region and the can (2,092.85W) and used the same properties everywhere in the geometry. The fourth simulation operated at $27.27\text{W}/\text{cm}^3$ in both the fueled region and the can, which gave about the same power (1,141.52W) as the first simulation. The fourth simulation also used the same properties everywhere in the geometry. Figure 32 shows the temperature profiles of the four simulations at a fluence of $1 \times 10^{25}\text{n}/\text{m}^2$. However, note that the first simulation includes thermal conductivity degradation of the can, whereas the other three simulations used Equation 19 for the thermal conductivity. In the first simulation, the thermal conductivity of the can using nominal values degraded to levels somewhat smaller than what would have been predicted using Equation 19. As a result, the maximum temperature of the first simulation was higher at a fluence of $1 \times 10^{25}\text{n}/\text{m}^2$ than when using the same properties in both the can and fueled region. The temperature of the third simulation was highest since it produced significantly more heat than the other simulations, and the maximum temperature of the fourth simulation was the smallest since it had the same heat produced as the first two and a shorter average distance for the heat transport.

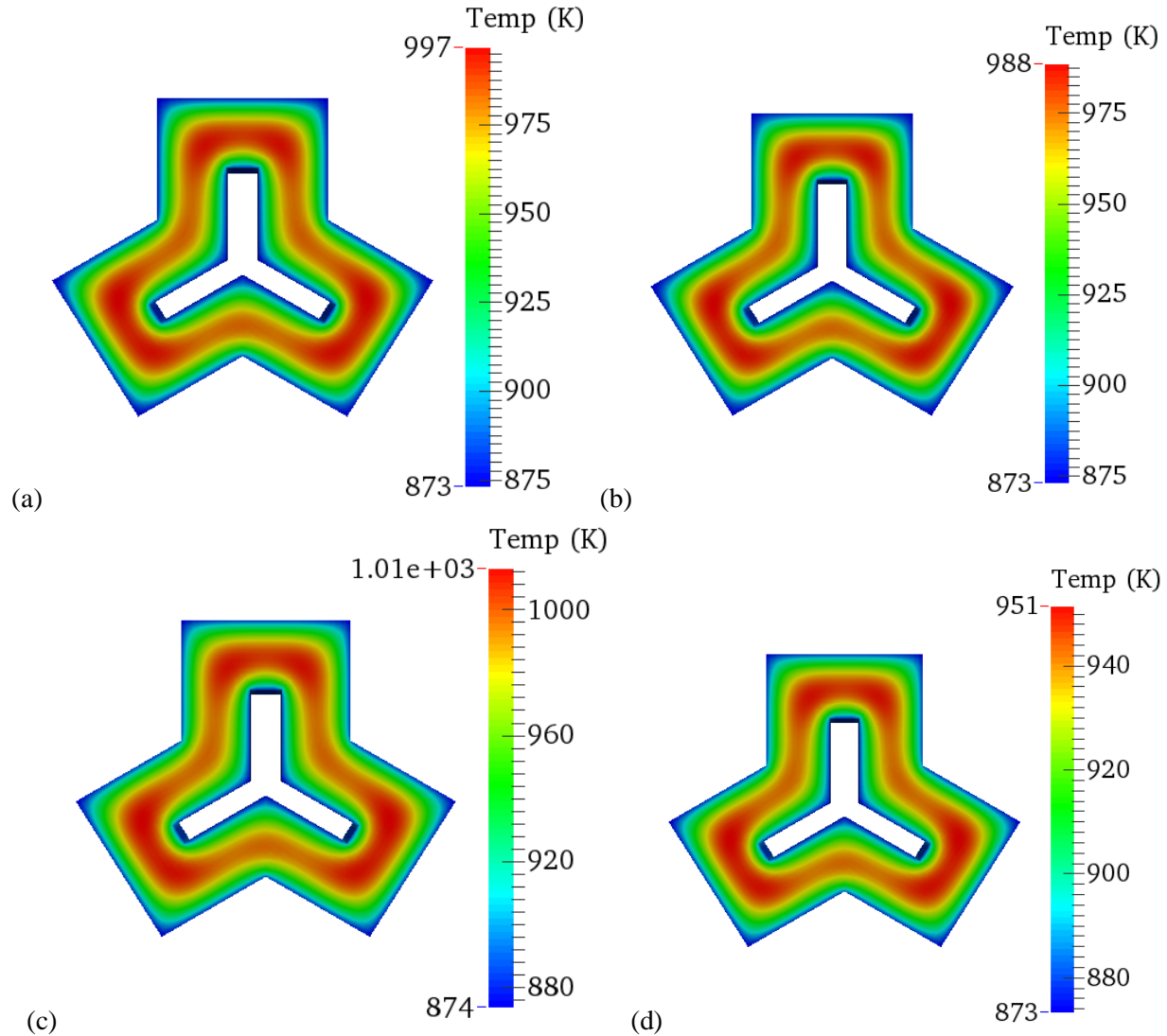


Figure 32. Temperature cross-section profiles of the Y mesh simulations at swelling saturation. (a) Temperature profile for the first simulation with nominal material values in the can and fueled regions. (b) Temperature profile for the second simulation with the same properties in both regions. (c) Temperature profile for heat generation in all regions at 50W/cm³. (d) Temperature profile for heat generation in all regions at 27.27W/cm³.

Figure 33 shows the maximum principal stress at the end of the power ramp. These stresses were due to the thermal expansion of the SiC. The maximum stresses due to thermal expansion followed the maximum temperature of the fuel. In the first simulation after the power ramp, the thermal conductivity of the can was greater than what would have been predicted using Equation 19, and, correspondingly, the maximum temperature was smaller (949K). As a result, the stress from thermal expansion was smaller than that predicted in Figure 33b. The previous figure shows the temperature profiles at a fluence of $1 \times 10^{25} \text{ n/m}^2$, whereas this figure shows the stresses after the power ramp.

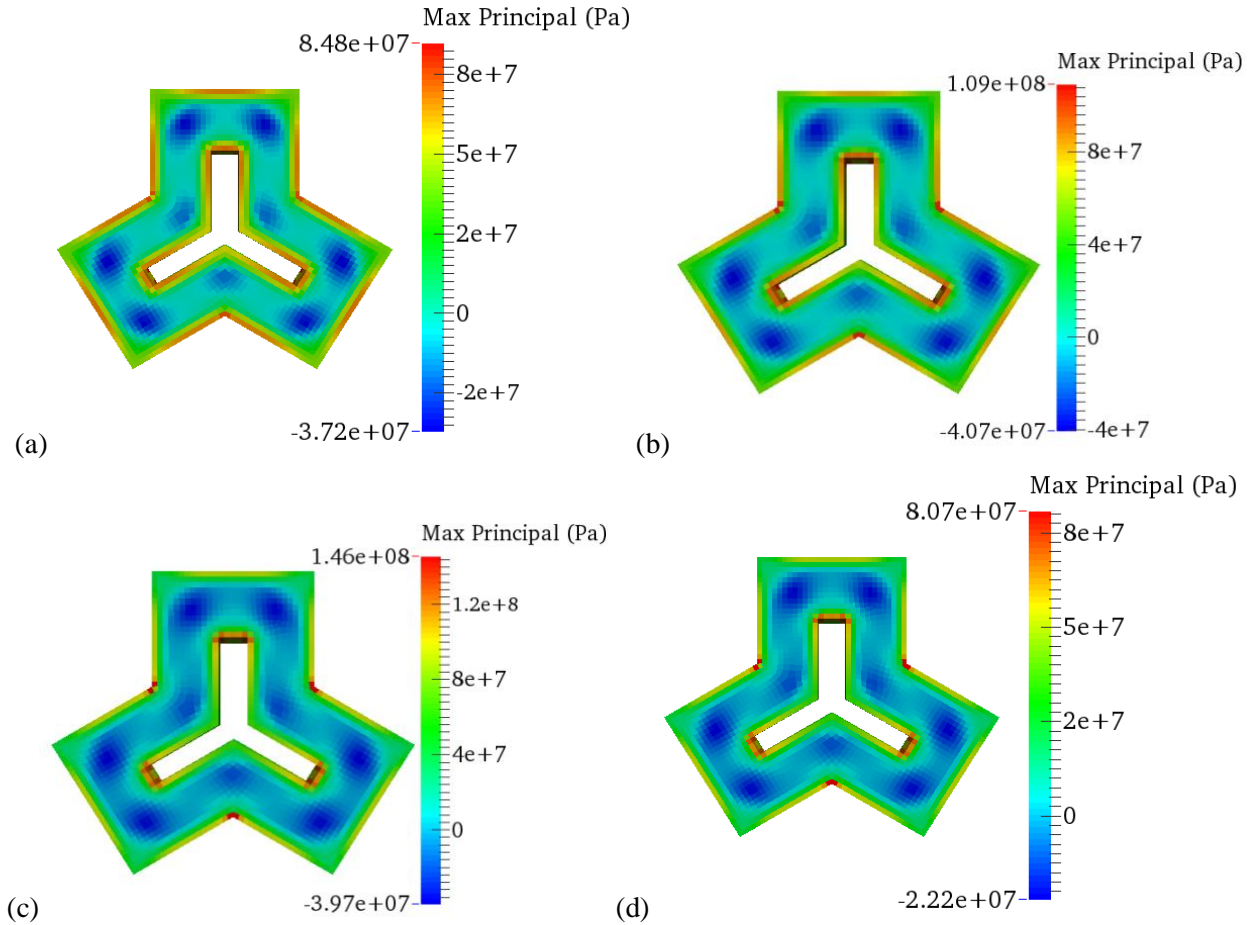


Figure 33. Maximum principal stress profiles at the end of the power ramp. (a) Stress profile for the first simulation with nominal material values in both regions. (b) Stress profile for the second simulation with the same material properties in both regions. (c) Stress profile for heat generation in all regions at $50\text{W}/\text{cm}^3$. (d) Stress profile for heat generation in all regions at $27.27\text{W}/\text{cm}^3$.

Figure 34 shows the maximum principal stresses at the end of the simulation and a fluence of $1 \times 10^{25}\text{n}/\text{m}^2$, which corresponds to about the fluence level needed for SiC swelling saturation. The stress profile in the first simulation showed a more uniform stress condition in the can compared with the other three simulations. However, the general profiles and stress magnitudes were similar. Additionally, the location of the maximum stress locations were the same in all four simulations.

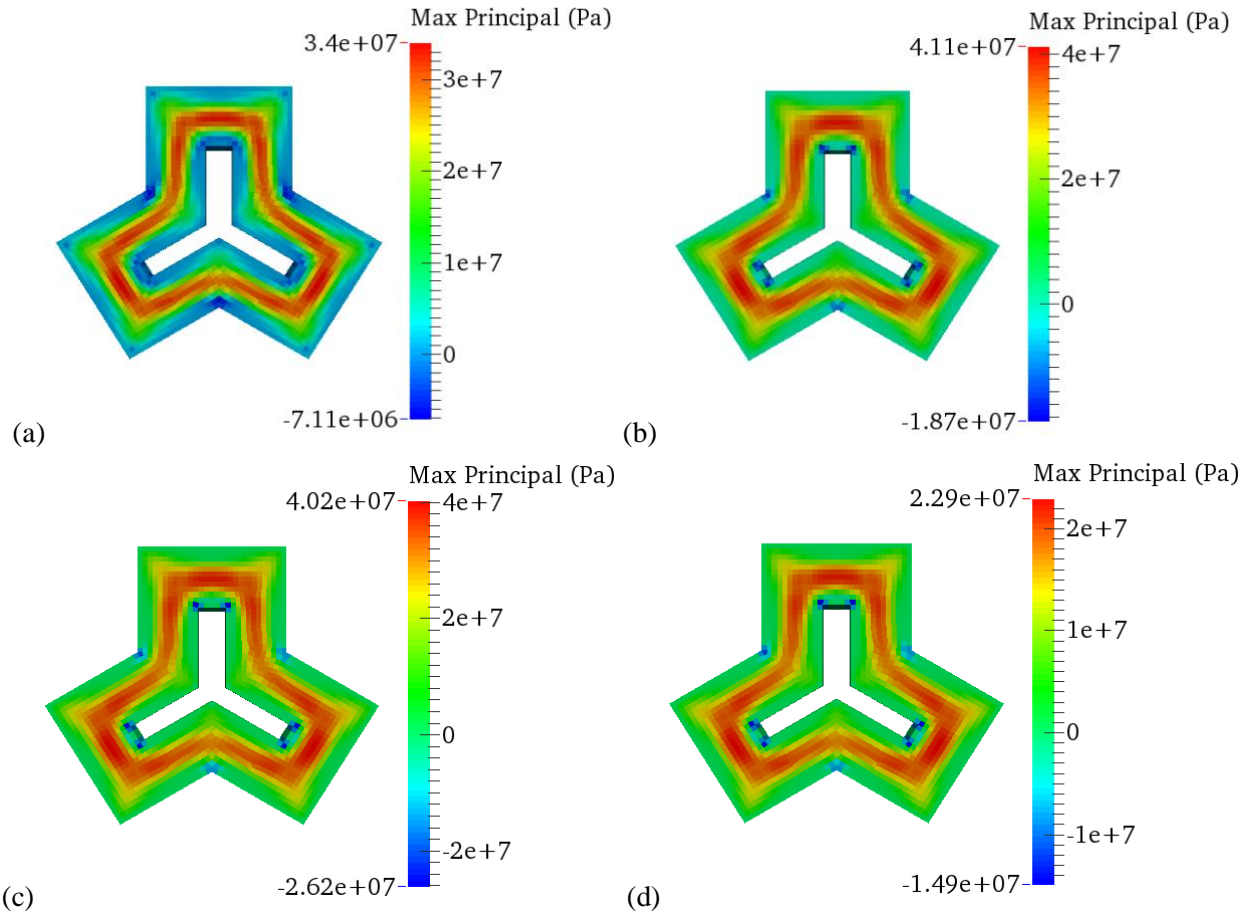


Figure 34. Maximum principal stress profiles at a fluence of $1 \times 10^{25} \text{ n/m}^2$. (a) Stress profile for the first simulation with nominal material properties. (b) Stress profile for the second simulation with the same material properties on both regions. (c) Stress profile for heat generation in all regions at 50W/cm^3 . (d) Stress profile for heat generation in all regions at 27.27W/cm^3 .

4.5.2 One-Dimensional Analysis

A 1D heat transfer check was performed to verify the general finding of the effect of power generation in can on centerline temperature. Two geometries were compared: one 6mm long with uniform heat generation and the other with a 5mm long region of heat generation with a 1 mm outer region between the heat generation and the coolant. The temperature profile in the geometry with uniform heat generation follows.

$$\frac{d^2T}{dx^2} = -\frac{q_1'''}{k} .$$

$$T = -\frac{1}{2} \frac{q_1'''}{k} x^2 + T_{max} .$$

$$T_{max} = \frac{1}{2} \frac{q_1'''}{k} 6e-3^2 + T_0 .$$

Then the maximum temperature of the nonheat generating region in the second geometry is given by

$$q'' = k \frac{\Delta T}{\Delta x} .$$

$$T_1 = T_0 + \frac{q'' \Delta x}{k} .$$

The temperature profile of the heat-generating region of the second geometry is given by

$$T = -\frac{1}{2} \frac{q_2'''}{k} x^2 + T_1 + \frac{1}{2} \frac{q_2'''}{k} 5e-3^2 ,$$

for values of

$$q_1''' = 5e7 \text{ W/m}^3 ,$$

$$q_2''' = 6e7 \text{ W/m}^3 ,$$

$$q'' = q_2''' * 5x10^{-3} \text{ m} = 3e5 \text{ W/m}^2 ,$$

$$k = 10 \text{ W/m-K} ,$$

$$T_0 = 873 \text{ K} ,$$

$$x_{centerline} = 0 \text{ m} .$$

Then the centerline temperatures are 963K for the uniform heat generation volume and 978K for the second geometry with a 1mm can between the heat-generating region and the coolant, which is consistent with the general BISON findings for equivalent power.

4.5.3 TRISO Cavities

To test the effects of simulating the SiC-fueled region with embedded TRISO particles as a homogenous material, a pellet with 106 cavities was generated and compared to a cylinder with the same outer dimensions. Figure 35 shows the simulated geometry of the pellet with the removed volume for TRISO particles. The pellet height was 4.5mm, and the diameter was 9.2mm. There were 106 TRISO volumes removed, each with a diameter of 1,130μm. The cavity fraction was 35% by volume, and the minimum distance between a TRISO cavity and an outer pellet surface was 35μm.

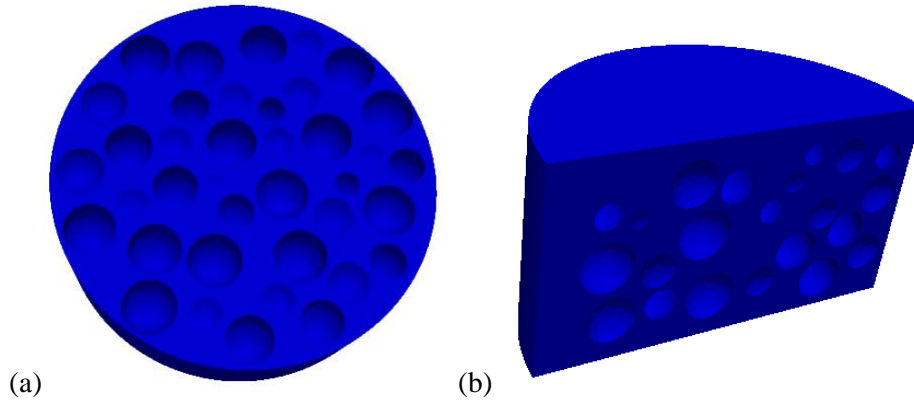


Figure 35. Geometry of the pellet with TRISO cavities.

The smear power density was set to $100\text{W}/\text{cm}^3$. This produced 24.34W in the cylinder geometry and 15.95W in the pellet with TRISO cavities. The fluence at the end of the simulation was $1 \times 10^{25}\text{n}/\text{m}^2$. Figure 36 shows the temperature and stress profiles from the TRISO cavity simulations. The results showed that the increased thermal resistance caused by the TRISO cavities produced a higher centerline temperature despite the smaller amount of power produced. Figure 36c and 36d show the maximum principal stress after the power ramp due to thermal expansion, and the stress in the simulation with the TRISO cavities is larger than the cylinder. This is due to the stress concentrations caused by the particles being in proximity to each other and the pellet outer surfaces. Figure 36e and 36f show the maximum principal stress at $1 \times 10^{25}\text{n}/\text{m}^2$, and similarly the stress in the TRISO cavity simulation is greater than in the solid cylinder.

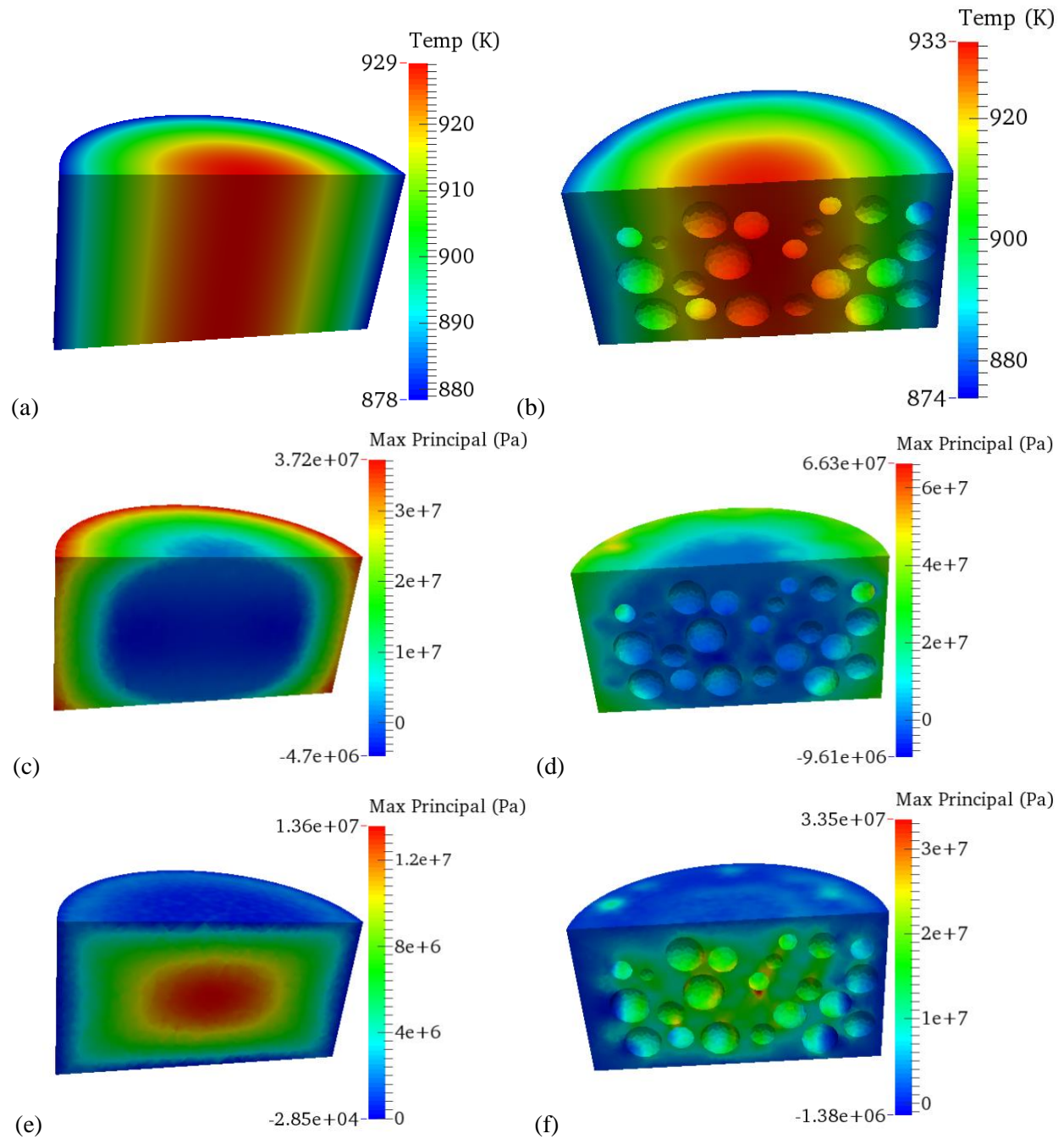


Figure 36. Plots of the temperature and maximum principal stress. Left is the solid cylinder results. Right are the results for the pellet with TRISO cavities. (a) and (b) Temperature profiles. (b) and (c) Stress profiles after the power ramp. (e) and (f) Stress profiles at swelling saturation.

5. CONCLUSION

Table 1 lists the material properties in order of their estimated effect on the stresses. The conclusions for the material property sensitivity studies of the SiC concept are that the swelling is the most important material property, followed by the elastic modulus. The thermal conductivity and the coefficient of thermal expansion also have an effect but not to the same level as the swelling and elastic modulus unless there is a far greater degree of uncertainty in the thermal expansion than expected. Poisson’s ratio has some effect on the stress in the fuel, but it is minor compared with the swelling and elastic modulus.

The conclusions for the SS316L sensitivity studies are that the thermal conductivity of the can is the most important followed by the elastic modulus and the CTE. The HTC’s of the side and bottom interface between the fuel and the can are somewhat important but to a lesser extent than the previous properties. Finally, Poisson’s ratio of SS316L is not important.

The conclusions for the geometry and modeling methods are that including additional detail such as a nonheat-generating SiC can and TRISO particle cavities does increase the accuracy of the simulation. However, the change in stress and temperature profiles is acceptable, and the change in magnitudes can be bracketed by the full power density throughout the entire volume and the equal total power cases. Thus, it seems reasonable to simulate fuel concepts as applicable using these simplifications, but additional accuracy can be obtained by simulating the geometry with a greater degree of realism.

Table 1. Ranking of significance of material properties to their effect on the stress.

Property	SiC Can and Fueled Region	SS316L and UO ₂
Thermal Conductivity	Moderate	High
Interface HTC Ratio	-	Moderately Low
Coefficient of thermal expansion	Moderately Low	Moderately High
Swelling	High	-
Elastic Modulus	Moderately High	Moderate
Poisson’s Ratio	Low	Insignificant

6. REFERENCES

- Allison, C. M., G. A. Berna, R. Chambers, E. W. Coryell, K. L. Davis, D. L. Hagrman, D. T. Hagrman, N. L. Hampton, J. K. Hohorst, R. E. Mason, M. L. McComas, K. A. McNeil, R. L. Miller, C. S. Olsen, G. A. Reyman, and L. J. Siefken. 1993. *SCDAP/RELAP5/MOD3.1 Code Manual, Volume IV: MATPRO A Library of Material Properties for Light Water Reactor Accident Analysis*. Idaho Falls: Idaho National Laboratory.
- Ben-Belgacem, M., V. Richet, K. A. Terrani, Y. Katoh, and L. L. Snead. 2014. “Thermo-mechanical Analysis of LWR SiC/SiC Composite Cladding.” *JNM* 447(1–3): 125–142.
- British Stainless Steel Association. “Elevated Temperature Physical Properties of Stainless Steels.” <https://www.bssa.org.uk/topics.php?article=139>.
- Fahr, D. 1973. *Analysis of Stress Strain Behavior of Type SS316 Stainless Steel*. ORNL-TM-4292. Oak Ridge: Oak Ridge National Laboratory.
- Fink, J. K. 2000. “Thermophysical Properties of Uranium Dioxide.” *JNM* 279(1): 1–18.
- Lucuta, P. G. 1996. “A Pragmatic Approach to Modeling Thermal Conductivity of Irradiated UO₂ Fuel: Review and Recommendations.” *JNM* 166–180.
- Mills, K. C. 2002. *Recommended Values of Thermophysical Properties for Selected Commercial Alloys*. Woodhead Publishing.
- Price, R. J. 1977. “Properties of SiC for Nuclear Fuel Particle Coatings.” *Nuclear Technology* 320–336.
- Rashid, Y., R. Dunham, and R. Montgomery. 2004. *Fuel Analysis and Licensing Code FALCON MOD01*. Electric Power Research Institute.
- Snead, L. L., T. Nozawa, Y. Katoh, T. Byun, S. Kondo, and D. A. Petti. 2007. “Handbook of SiC Properties for Performance Modeling.” *JNM* 371(1): 329–377.
- Trammell, M. P., B. C. Jolly, M. D. Richardson, A. T. Schumacher, and K. A. Terrani. 2016. *Advanced Nuclear Fuel Fabrication: Particle Fuel Concept for TCR*. ORNL/SPR-2019/1216, M3CT-19OR06090130, Oak Ridge: Oak Ridge National Laboratory.
- United Performance Metals. “Stainless 316, 316L, 317, 317L.” <https://www.upmet.com/sites/default/files/datasheets/316-316l.pdf>.
- Williamson, R. L., J. D. Hales, S. R. Novascone, M. R. Tonks, D. R. Gaston, C. L. Permann, D. Andrs, and R. C. Martineau. 2012. “Multidimensional Multiphysics Simulation of Nuclear Fuel Behavior.” *JNM* 423(1): 149–163.